Pyrrolic nitrogen-doped multiwall carbon nanotubes using ball-milled slag-SiC mixtures as a catalyst by aerosol assisted chemical vapor deposition

To cite this article: Sofía Magdalena Vega-Díaz *et al* 2020 *Mater. Res. Express* **7** 025602

View the article online for updates and enhancements.

Materials Research Express

Pyrrolic nitrogen-doped multiwall carbon nanotubes using ball-milled slag-SiC mixtures as a catalyst by aerosol assisted chemical vapor deposition

Sofía Magdalena Vega-Díaz[1] , Viviana Jehová González[2] , Aarón Morelos-Gómez[3] ,
Ferdinando Tristán-López[4] , Gladis Judith Labrada-Delgado[5] , Beatriz Adriana Rivera-Escoto[5] ,
Roque Sánchez-Salas[5] , Alejandro Javier Cortés-López[5] , Juan Luis Fajardo-Díaz[5] ,
Florentino López-Urías[5] , Mauricio Terrones[6] and Emilio Muñoz-Sandoval[5,7]

[1] Catédras-CONACYT-Instituto Tecnológico de Celaya, Avenida Tecnológico esquina con García Cubas S/N, CP 38010, Guanajuato, México
[2] Departamento de Ciencia e Ingeniería de Materiales e Ingeniería Química, Universidad Carlos III, Av. Universidad 30, 28911 Leganés, Madrid, Spain
[3] Global Aqua Innovation Center, Shinshu University and Research Initiative for Supra-Materials, 4-17-1 Wakasato, Nagano-city 380-8553, Japan, Shinshu University, 4-17-1 Wakasato, Nagano-city 380-8553, Japan
[4] Departamento de Ciencias Naturales e Ingeniería, Metropolitan Autonomous University, Av.Vasco de Quiroga 4871, Colonia Santa Fe Cuajimalpa, Delegación Cuajimalpa de Morelos, Distrito Federal, C.P. 05300, México
[5] Advanced Materials Division, IPICYT, Camino a la Presa San José 2055, Col. Lomas 4a, San Luis Potosí, SLP, 78216, México
[6] Department of Physics, Department of Chemistry, Department of Materials Science and Engineering and Center for 2-Dimensional and Layered Materials, The Pennsylvania State University, 104 Davey Lab., University Park, PA 16802-6300, United States of America
[7] Authors to whom any correspondence should be addressed.

E-mail: ems@ipicyt.edu.mx

Keywords: N-pyrrolic, slag, SiC, carbon nanotubes

Supplementary material for this article is available online

Abstract

We demonstrated that the ball-milled slag-SiC mixture is an effective catalyst to grow pyrrolic nitrogen-doped multiwall carbon nanotubes (N-MWCNTs) by aerosol assisted chemical vapor deposition (AACVD) method. N-MWCNTs synthesized at 800 °C, 850 °C and 900 °C were characterized by scanning electron microscopy (SEM), transmission electron microscopy (TEM), Raman spectroscopy, x-ray powder diffraction (XRD), and x-ray photoelectron spectroscopy (XPS) and thermogravimetric analysis (TGA). TEM characterizations revealed the presence of a bamboo-like structure, a typical feature of nitrogen-doped carbon nanotubes. The presence of nitrogen was confirmed by the N1s XPS spectrum. Furthermore, a deconvolution of the N1s spectra revealed the presence of N-pyrrolic defects. This nitrogen functionality is investigated concerning the presence of silicon carbide material. Giant nanotubes with large diameters were obtained when SiC was added to the slag to be used as a substrate for N-MWCNTs synthesis. From Raman spectroscopy, the appearance of the D-band was observed, indicating the presence of topological defects that were also observed by TEM. XRD and TEM characterizations demonstrated the presence of Fe_3C and α-Fe nanoparticles. The N-MWCNTs fabricated here could be used into (electro)catalytic applications or for reinforcing ceramic nanomaterial or polymers.

1. Introduction

Carbon nanotubes (CNTs) possess outstanding physical, electronic, and mechanical properties [1]. They have been used to manufacture supercapacitors [2, 3], catalytic electrodes [4], superhydrophobic coatings [5], biomimetic surfaces [6], artificial muscles [7], integrated microelectromechanical systems [8], chemical sensors [9], field emitters [10–12], graphene-like materials [13–16], and bio-nanomedicine-related devices [17]. The commonly used methods to synthesize CNTs are arc discharge [18], laser ablation [19], and chemical vapor

deposition (CVD) [20]. The CVD technique consists of the pyrolysis of hydrocarbons in the presence of catalytic metal nanoparticles under an inert atmosphere. Two main growth mechanisms of CNTs have been reported: tip and root growth [21–23]. CNTs can be doped with nitrogen [24], co-doped with nitrogen and phosphorus [25], and decorated with oxygen functional groups [26]. Other chemical elements can be incorporated into the lattice of CNTs, such as boron [27–29], silicon [30], and sulfur [31].

Metal nanoparticles have played a crucial role in growing CNTs by the CVD technique; among the most used metals are Fe [32–34], Co [35], and Ni [36–38]. However, metal transition carbide nanoparticles inside CNTs have also been found [39–41]. Encapsulated ferromagnetic nanoparticles in doped CNTs exhibit high coercive fields when compared to ferromagnetic nanoparticles encapsulated inside of un-doped CNTs [41]. Some salts, such as K_2CO_3 and Li_2CO_3, have been used as catalysts in the production of CNTs [20]. Other chemical elements and compounds have also been used as catalysts in the synthesis of carbon nanostructures [42–45]. It has been reported that it is possible to grow CNTs using clay [46, 47] or volcanic lava stones as a catalyst [48–50].

Nitrogen has been playing a crucial role in different carbon nanostructures, mainly in carbon nanotubes, for example, to improve the electrocatalytic activity for oxygen reduction reactions [51]. Nitrogen-doped multi-walled carbon nanotubes (N-MWCNTs) have shown to possess unique electrical properties [52]. Investigations have demonstrated that nitrogen atoms are mainly bonded to carbon in pyridine, pyrrolic, or graphitic configurations [52]. In the N-graphitic case, it is presumed that the materials present an n-type semiconductor behavior. N-pyrrolic most likely increments the concentration of electrons due to the pentagonal rings and the sp^3 hybridization, like what has been observed in graphene by Li *et al* [53]. Other researchers found that N-pyrrolic could be a source of magnetism in graphene [54]. Ombaca *et al* [55] reported that N-pyrrolic configuration in carbon nanotubes improves the palladium catalytic properties because it introduces a better catalytic activity in the carbon material. Bulusheva *et al* [56] synthesized N-MWCNTs by AACVD method using ferrocene as catalytic precursor and benzylamine or acetonitrile as nitrogen and carbon precursors. Their results revealed that the concentration ratio N/C is determinant for how the nitrogen is incorporated into the lattice of carbon nanotubes. For an N/C ratio of less than four, all types of N configurations can be obtained. For larger values of the N/C ratio, the nitrogen is found in a molecular fashion. Huang *et al* [57] reported that the catalytic activity of carbon materials depends on the nitrogen content. They also found that N-pyrrolic is the most effective to increase catalytic activity. Recently, Zheng *et al* [58] synthesized N-MWCNT using exotic materials and ball milling procedures. They used biomass to fabricate N-MWCNTs, which were very useful for its electrocatalytic activity for oxygen reduction reaction (ORR). Furthermore, N-MWCNTs exhibit outstanding chemical [59], physical [60, 61], and even biocompatible [62] properties when compared to undoped CNTs. They have recently been studied for their high electrocatalytic activity [63].

In relation to the silicon carbide SiC material involved in the CNT growing, Murakami *et al* [64] fabricated well-aligned metallic and semiconductor SWCNTs using a Fe-Co contaminated 6H-SiC as catalyst-substrate by catalytic CVD (CCVD). Using a floating-catalyst CVD method Ci and Bai [65, 66] fabricated MWCNT on SiC particles. They employed a ferrocene-xylene mixture as feedstock for producing the CNTs. They showed that the SiC/CNT's hybrid particles could be utilized as suitably reinforced composites. It has been also demonstrated that SiO_2 could help to grow CNT on SiC via Fe catalyst nanoparticles [67]. The use of xylene [68, 69], acetylene [70], toluene-ethanol mixtures [71] and ferrocene to grow CNT on SiC nanostructures has been employed for diverse groups. It has been demonstrated that oxygen improves the growth of CNT [71]. All of these research works used as a source of catalyst ferrocene by a CVD method. However, there are also reports about the growth of CNT using SiC nanoparticles on Si substrates [72]. They proposed that the curvature at the nanoscale level is enough to grow CNTs. They used SiC nanoparticles formed on Si(111) substrate. Also, SiC composites have been proposed to reinforce alumina ceramic nanomaterials [72, 73] and to obtain materials with large electrical conductivity [74]. By a high-temperature CVD, Matsuda *et al* [75] fabricated thin high dense and aligned CNT film on SiC substrates.

In the case of slag, it is composed of several materials and could be used as an ornament or for remediation of eroded areas. In most cases, slag is simply discarded. Therefore, recycling this product is essential since it may contain possible contributions to novel industrial applications. The composition of the slag depends on the kind of soil and processes used to extract materials from mines. Diverse materials artificially incorporated in the substrate for CNT production can promote unusual morphologies with many active sites for multiple applications [76, 77]. One of the primary materials that compose the slag is SiC, which, combined with Fe, could give a unique catalyst to produce carbon nanomaterials. Through this investigation, we report a low-cost method to produce N-pyrrolic N-MWCNTs using ball-milled slag-SiC mixtures nanomaterial by the AACVD method. The slag materials used in this work were obtained from the waste of a copper mine. To the best of our knowledge, there is no report on the use of slag (or slag-SiC mixture) as a catalyst and liquid hydrocarbons as a precursor for the synthesis of N-MWCNTs using the AACVD method.

2. Experimental

The slag material used in this work comes from Minera Mexico, a mining industry located in San Luis Potosí, Mexico. As–received slag was grounded as follows: the slag was immersed in liquid nitrogen and hit with a hammer to reduce the size of the material; later, they were ground in a mortar to produce fine powder material. Following this, the resulting powders were sieved through a 32 microns mesh, and 4.5 grams of these powders were introduced into milling steel vials (6.4 cm high and 5 cm outer diameter and 3.3 cm internal diameter) together with 12 ml of ethanol and crushed for 120 min. The steel balls were four of 6.33 mm diameter and four of 12.7 mm diameter. The resultant slag particles exhibited sizes ranging from 100–500 nm long. This sample is denoted as SG-2h. Another ball-milled powder sample was obtained by adding 0.045 grams of SiC (K D Unipress) to the 4.5 grams of slag. The same milling procedure was performed in this sample. This sample was called SG-SiC. N-MWCNTs were synthesized by the AACVD method [24] using SG-2h or SG-SiC nanoparticles. The figure S1 is available online at stacks.iop.org/MRX/7/025602/mmedia (supplementary information) shows a drawing of the CVD setup used in this work. Two different procedures were employed to fabricate three different kinds of N-MWCNTs, as following: (1) one procedure consisted of a mixed solution of benzylamine ($C_6H_5CH_2NH_2$, Sigma-Aldrich, 99%) with 6% by wt. of SG-2h for the sprayer. This mixture is subjected to an ultrasonic bath for 30 min to obtain a well-homogenized solution. The final solution is then introduced into the ultrasonic mist generator. An aerosol cloud is generated and carried by argon flow (Praxair 99%), which flows at a rate of $2.5 \, l \, min^{-1}$ through a quartz tube (1 inch and 1.1 inch are the internal and external diameters, respectively). Such quartz tube is inside a tubular furnace where N-MWCNTs are grown (see figure S1); (2) the second procedure involved two kind N-MWCNTs, these consisted in placing the SG-2h (or SG-SiC) inside the quartz tube within the first furnace, then benzylamine alone was introduced into the ultrasonic mist generator, and the synthesis was carried out. In the three cases, the synthesis was done at three different temperatures (800 °C, 850 °C, and 900 °C). The samples were labeled as CNx-800, CNx-850, and CNx-900 for the procedure (1), and the other two kinds of samples obtained by the procedure (2) were labeled as CNx-T-SG when SG-2h was used as catalyst, and when SG-SiC was used the samples where CNx-T-SiC (T = 800 °C, 850 °C and 900 °C). A detailed scheme of the N-MWCNT fabrication process can be seen in figure S2. Samples were dispersed using a Cole Palmer ultrasonic processor (500 watts 20 kHz) for the characterization. The produced N-MWCNTs were characterized by SEM, scanning transmission electron microscopy (STEM), and energy dispersive spectroscopy (EDAX) using a Philips FEG-XL30 microscope and an HRTEM 300 kV FEI TECNAI F30 STWIN G2. X-ray powder diffraction patterns (XRD) were obtained using a Bruker XD8 ADVANCE, and Raman spectra were obtained using a Micro Raman Renishaw with excitation wavelengths of 633 nm and 532 nm. X-ray photoelectron spectroscopy was performed using a PHI 5000 VersaProbe II equipment with a monochromatic Al-$\kappa\alpha$ source (1486.7 eV). The deconvolution analysis was performed using the software Spectral Data Processor SDP 4.1. In addition, thermogravimetric analysis (TGA) was performed for all samples using an STA 6000 Perkin-Elmer under the following conditions: samples were heated in simultaneous thermal analyzer in a temperature range of 50 to 950 °C with a heating speed of $10 \, °C \, min^{-1}$ under a dynamic flow of oxygen ($20 \, ml \, min^{-1}$). Measurements of CNT diameter were obtained using ImageJ (free software for image analysis from the National Institutes of Health) from at least 5 SEM (50,000X) images of each sample. Crystallographic Toolbox software was used to obtain zone-axis analysis and diffraction pattern recognition.

3. Results and discussion

3.1. SEM characterization

Energy dispersive x-ray (EDX) spectra revealed the existence of several chemical species in the slag, SG-2h, and SG-SiC (see figure 1). Nine elements could be detected; oxygen (O), silicon (Si), iron (Fe), calcium (Ca), copper (Cu), aluminum (Al), molybdenum (Mo), magnesium (Mg) and potassium (K). Figure S3 shows SEM images and the nanoparticle size of SG-2h, showing a bimodal size.

Although the results of EDX analysis performed on the samples are only qualitative, they can be served as a guide for the analysis. For example, from table 1, considering the case of slag without SiC, the Fe content is around 10 at%. However, when the SiC was added, it seems that Fe concentration is relatively reduced to ~3 at % with higher concentrations of oxygen (~45%), and Si concentration near to the 10%.

Figure 2 shows the elemental mapping of the main detected chemical elements that were performed on a particle of SG-2h. Notice that all considered elements are homogeneously distributed on this sample. XRD patterns of the original slag, SG-2h, and SG-SiC also were performed, observing the presence of silicon carbide (SiC), magnetite (Fe_3O_4), iron carbonyl sulfide ($Fe_3(CO)_{10}S$) among other more complex crystal structures (see figures S4(a)) and (b)).
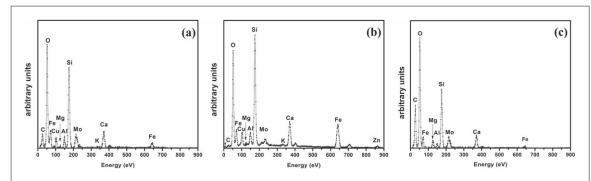
Figure 1. Energy-dispersive x-ray spectroscopy (EDX) chemical analysis of slag before ball milling process (a); 2 h ball-milled slag material (b); and 2 h ball-milled slag + SiC mixed material. Apparently, the main contributions in the (a) and (b) cases come from Fe, O, Si, and Ca. In the case of (c) also C seems to have a significant contribution.
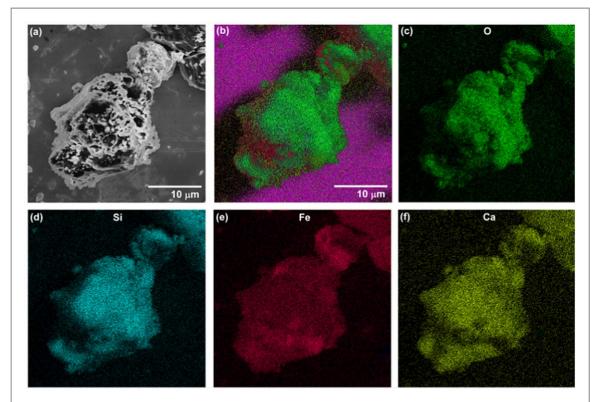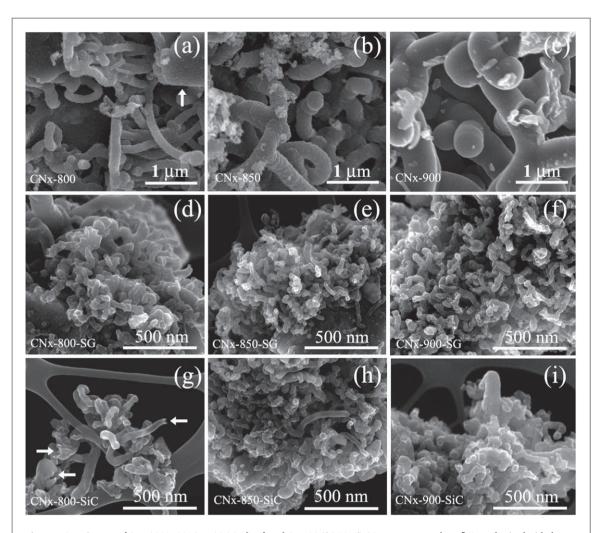

Figure 2. SEM images and EDX elemental mapping of ball-milled slag for 120 min. The main mapped elements are oxygen (c), silicon (d), iron (e), and calcium (f). A superposition of all chemical elements is shown in (b).

Table 1. Chemical elemental quantification detected by EDS measurements for slag material milled for 0 and 120 min. In addition, the results for slag-SiC material is exhibited in the 120(SiC) file. The presence of O, Si, and Fe is remarkably outstanding.

Element Time of milling (min)	Atomic concentration (at%)							
	O	Si	Fe	Ca	Cu	C	Mg	Al
0	43.38	15.35	11.33	6.46	2.35	19.21	0.21	1.70
120	36.30	12.78	8.17	6.29	0.94	33.44	—	2.07
120(SiC)	43.39	8.66	2.92	4.19	—	39.17	1.17	0.50

When the SG-2h material is mixed with benzylamine to synthesize N-MWCNTs, the effect of synthesis temperature is very important to define the carbon nanotube diameter. For example, the average diameter observed in CNx-800 (figure 3(a)) is found in the range of 20–60 nm, but some larger diameter can be observed (see the white arrow and figure S5(a)). However, when the temperature of synthesis rises to 850 °C (figure 3(b)),

Figure 3. SEM images of CNx-T (a)–(c), CNx-T-SG (d)–(f) and CNx-T-SiC (g)–(i) (T = 800, 850 and 900 °C) synthesized with the CVD method at synthesis temperatures of 800 °C (a), (d), (g), 850 °C (b), (e), (h) and 900 °C (c), (f), (i).

the diameter distribution is bimodal with diameters around 330 nm and 580 nm (figure S5(b)). At 900 °C, the CNx-900 possesses large diameters around 400 nm and 600 nm (figure 3(c)), but also a smaller diameter near 100 nm (figure S5(g)). It is possible to observe Y junctions and branches or kinks, which could be due to the presence of sulfur contained in the SG-2h. Previous experimental reports demonstrated that sulfur induces branched or Y-shaped morphologies in MWCNTs [31, 78].

A completely different morphology is found when the SG-2h is placed in the quartz tube for the N-MWCNTs synthesis. Although CNx-800-SG (figure 3(d)) presents a variety of diameters from 20 nm to 160 nm, most of them have diameters less than 100 nm. At this temperature, the size of the catalytic nanoparticles is not uniform, and the diameter of CNx-800-SG also did not present a preferential size. When the temperature is raised to 850 °C (figure 3(e)), the distribution of CNx-850-SG diameter exhibits a Lorentzian-like distribution with a peak around 30 nm (figure S5(e)). If the temperature is increased to 900 °C (figure 3(f)), the diameter distribution of CNx-900-SG is also Lorentzian-like with a peak at 70 nm (see figure S5(h)).

The morphology of CNx-850-SG (figure 3(e)) is like the CNx-800-SG but with a larger diameter probably as a consequence of a higher temperature synthesis. In the case of CNx-900-SG (figure 3(f)), the surface is damaged. It is observed that some of them appear to be longitudinally cut. Although this CNx-T-SG (T = 800 °C, 850 °C, 900 °C) group of N-MWCNTs presents many defects, they have a uniform appearance at these SEM images.

The morphologies of the CNx-T-SiC group (T = 800 °C, 850 °C, 900 °C) are similar to the CNx-T-SG group of N-MWCNTs, but some peculiarities deserve to be mentioned. For example, in figure 3(g) (CNx-800-SiC case), there are open carbon nanostructures (white arrows) with non-uniform diameters. There are also many agglomerates of N-MWCNTs. The same circumstance happens with CNx-850-SiC and CNx-900-SiC, figures 3(h), and (i), respectively. It is worth mentioning that in the case of CNx-T-SG and CNx-T-SiC, the carbon nanotubes are regularly attached to the catalyst substrate (~2 or 3 μm of size). It is probably that some irregular morphologies of CNx-T-SiC are due to the additional SiC powder in slag. It is possible that SiC
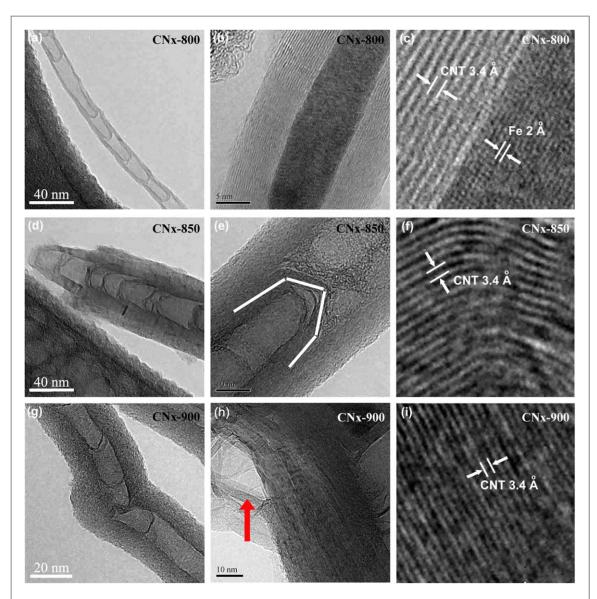
Figure 4. Transmission electron microscopy (TEM) images showing the CNx nanostructures obtained using SG-2h and benzylamine mixtures. The different CNx-T groups of samples were synthesized at (a)–(c) 800 °C, (d)–(f) 850 °C, and (g)–(i) 900 °C. The bamboo-shape morphologies of N-MWCNTs are obtained due to the presence of nitrogen. In all cases, the spacing of the graphite layers is 3.4 Å.

powders interacted with traces of Fe, O, Ca, Cu, Al, Mo, and Mg, forming a complex catalyst that provokes the formation of atypical N-MWCNTs.

3.2. TEM characterization

The TEM image of CNx-800 (see figure 4(a)) confirmed the presence of the typical bamboo-like feature, as previously reported [77]. Figure 4(b) displays a nanoparticle inside of a CNx-800. The presence of the graphitic layers with an interlayer spacing of 3.4 Å and iron-carbide nanoparticle reveals an interlayer spacing of 2 Å, which corresponds to the (200) plane of Fe_3C (figure 4(c)). We observed that CNx-800 exhibited large catalytic nanoparticles, which were found mainly within nanotubes with relatively small diameters (around 20 nm). Figure 4(d) shows bamboo shape N-MWCNts from CNx-850 exhibiting a broken tip. It can be observed that compartment dimensions in the bamboo-shape structures change alongside the CNT. Figure 4(e) shows the structure of borders between compartments. The acute geometrical structure observed could be explained due to the possible existence of N-pyrrolic chemical species. The typical distance of 3.4 Å between graphitic layers is shown in figure 4(f). For a synthesis temperature of 900 °C, in CNx-900 sample kink morphologies were identified (figure 4(g)), these morphologies could be attributed to deficient concentrations of non-carbon elements such as sulfur [78,79]. However, in some cases, the produced CNx-900 exhibits a poor graphitization on the walls (see figure 4(g)). This effect could be generated due to the multi-element catalyst precursor. It is well known that defects close to the surface of CNTs that contain foreign atoms can present such behavior in the
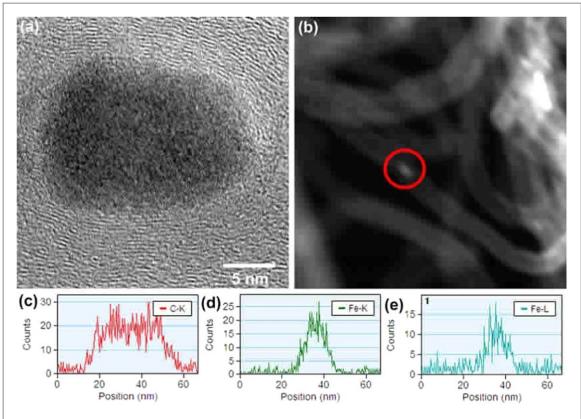
Figure 5. (a) HRTEM image of a nanoparticle inside a CNx-900; (b) Scanning transmission electron microscopy (STEM) image of (a); EDX line profile along the nanoparticle for (c) C-K, (d) Fe-K, and (e) Fe-L.

carbon walls [52]. Nevertheless, some of the CNx-900 presents very well graphitization, as it is shown in figure 4(h), although superficial cavities also are formed (red arrow). The distance between the carbon layers was 3.4 Å in this sample.

To identify the chemical elements contained in the catalytic particles, we performed an energy dispersive spectra (EDS) line profile of different nanoparticles inside CNx-900 (see figures 5(a) and (b)). The EDS line profiles indicate that the nanoparticles contain mostly Fe (see figures 5(d) and (e)). The carbon line profile does not exhibit a significant drop in the intensity. This fact suggests that the interior of the nanoparticle is composed of iron carbide (Fe_3C).

Figure 6 shows TEM images of different features of CNx-800-SG nanomaterial. Figure 6(a) shows a cluster of nanoparticles that were agglomerated in apparently amorphous carbon material. It is possible to observe a carbon flake below the cluster (red arrow). Figure S7(a) exhibits the same cluster but with a blue circle to point the zone where an EDX chemical analysis was performed (figure S7(b)). Notice that almost the same elements of original slag were detected. In figure 6(b), an irregular small diameter CNT entangled with a curved large-diameter CNT. Note that two large nanoparticles (red arrows) could be responsible for such complex amassment. The inset (red square) in this figure shows another example of this structure; in this case, there are four nanoparticles involved (yellow arrows). This type of morphology seems to be a constant when the SG-2h is set into the quartz tube for the CNT synthesis. Two kinds of nanotubes could be mainly detected. One with a large external diameter (∼130 nm) and relatively small thickness of multiwall carbon layers (∼30 nm). The relation between the outer diameter (O.D.) divided by internal diameter (I.D.) being more than four. It is possible that these kinds of CNT (red arrow in figure 6(c)) are generated by large nanoparticles. Interestingly, in some areas of N-MWCNT nanostructure, there are double or triple groups of multiwall carbon layers (see yellow arrow in figure 6(c)). The bamboo shape of this giant N-MWCNTs is not uniform, and mostly the compartments are divided by few carbon layers. Another kind of structure found is shown in figure 6(d), where an irregular tubular curved carbon nanostructure is exhibited. The rugged surface of this kind of CNT is severely affected due to small nanostructures that are attached (red arrows in figure 6(d)). A closer image shows such surface nanostructures (red arrows in figure 6(e)). Besides, the carbon walls are only locally ordered and have a thickness around 17 nm, considering that the diameter of the nanotube is ∼35 nm, then O.D./I.D.∼2. This morphology property promotes irregular compartments (figure 6(e)).

The encapsulated nanoparticle observed in figure 6(d) (red circle) is α-Fe (see inset of figures 6(f) and S8) with spheroidal-shape (figure 6(f)). The inset of this figure is the FFT that define a [−110] zone-axis . Figure 6(f)
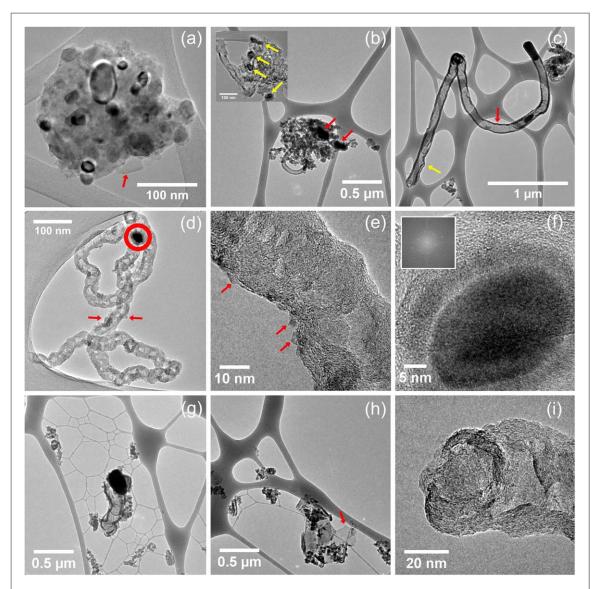
Figure 6. TEM and HRTEM images showing different CNx-800-SG nanostructures observed. (a) Agglomeration of nanoparticles immerses in carbon nanomaterial. (b) Aggregation of small diameter curved CNx-800-SG; the inset shows nanoparticles in this entangled CNTs. (c) individual large-diameter CNx-800-SG with a double group of walls and at the tip. (d) Individual small diameter curved CNx-800-SG with the rugged surface. (e) Structure of the surface of CNx-800-SG showed in (d), note the no uniform internal cavities of this kind of CNT. (f) HRTEM of a catalytic nanoparticle surrounded by iron oxide (see text). (g) Low magnification TEM showing an enormous diameter CNx-800-SG, the catalytic nanoparticle is around 300 nm large. (h) Several small diameter CNx-800-SG adhered to an unfolded carbon nanotube. (i) Tip of a small diameter curved CNx-800-SG, where it was probably occupied by a catalytic nanoparticle.

shows a faint ring surrounded the nanoparticle. This ring is associated with iron oxide [80], but here according to the EDX results, this ring probably also contains SiO_2 (see figure S9). Figure 6(g) is a TEM image exhibiting another short CNx-800-SG with a large diameter (∼250 nm). Due to the active sonication process, it is very likely that some of these CNTs with large diameters were unzipped, yielding graphite sheets of few layers (see red arrow in figure 6(h)). Notice that although the structure of CNx-800-SG of figure 6(e) is not uniform, the carbon layers exhibit a good grade of crystallinity (figure 6(i)).

The effect of raising the synthesis temperature to fabricate CNx-850-SG is shown in figure 7. The clusters of curled CNx-850-SG (figure 7(a)) are present. At this temperature of 850 °C, the catalytic nanoparticles are spherical and larger. This morphology is regularly not present in typical N-MWCNTs synthesis with benzylamine and ferrocene, where the catalyst nanoparticles are conical and more abundant [80]. The carbon structures shown in figure 7(b) are present in almost all temperatures of CNx-T-SG (T = 800, 850, and 900 °C). The majority of these CNTs exhibit irregular kink structures and no homogeneous compartments in size and shape (figure 7(c)). The presence of non-carbon elements, such as sulfur or nitrogen, could induce this irregular morphology [31]. Note, however, that the crystalline of CNx-850-SG is apparently not affected. It could be detected 200 nm-diameter CNx-850-SG with curly surface and large tip catalyst (see red arrow in figure 7(d)). In addition, long nanotubes without bamboo shape also were found (yellow arrow in figure 7(d)). Fe_3C
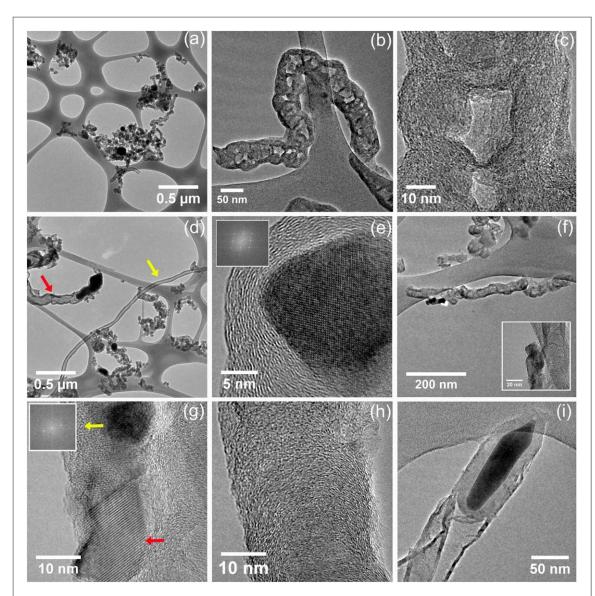
Figure 7. TEM and HRTEM images of CNx-850-SG. (a) Agglomeration of small diameter CNx-850-SG. (b) Single small diameter curved CNx-850-SG, similar to CNx-800-SG case (figure 6(d)). (c) Cavities of such CNx-850-SG with large walls. (d) Large diameter CNx-850-SG with a corrugated surface. (e) HRTEM of Fe$_3$C nanoparticle with [011] zone-axis , the inset is the respective FFT. (f) Large nanoparticle attached to CNx-850-SG, the inset shows a close view. (g) The HRTEM image of this attached nanoparticle which is composed of two smaller nanoparticles being both Fe$_3$C with different zone-axis (see figures S13 and S14). (h) A collapsed CNx-850-SG was forming a nanoribbon. (i) A TEM image of a large nanoparticle.

nanoparticle encapsulated within the nanotubes were observed (figure 7(e)) with a [011] zone-axis . Figure S10 shows the general procedure to define the zone-axis, and the crystal structure is displayed. In figure S11, its respective EDX analysis is presented; notice that the Fe and C peaks are the most intense. Another aspect of this CNx-850-SG is the small attached material to the outer walls (figure 7(f) and inset), which exhibit a more complex morphology. CNx-850-SG also contains several kinds of nanoparticles that probably were partially responsible for its irregular morphology. The inset of figure 7(g) corresponds to the FFT (yellow arrow) of Fe$_3$C nanoparticle, in which the [0–23] crystal direction could be identified (see figure S12). Figure S12 shows the complete analysis carried out for the identification of this crystal direction and the crystal structure of this internal Fe$_3$C nanoparticle. High crystallinity of Fe$_3$C (red arrow) nanomaterial is observed in the inferior part of the same figure 7(g) with distances of ~2.4 Å and ~4.8 Å. Figure S13 also shows the whole analyses performed on this nanomaterial to determine the crystal structure associated with the TEM image were the crystall plane was [010]. The EDX analysis is shown in figure S14(b), where several elements were detected. It looks that the O, Si, Ca, Mn elements could be a component of the material around such Fe$_3$C nanoparticles (see figure S14(a)). Some carbon nanoribbon-like structures were also observed (figure 7(h)). Figure 7(i) exhibits another large CNx-850-SG with 100 nm of diameter and a large catalyst nanoparticle presenting a sharp end. This nanoparticle is covered with a wide graphitic shell.
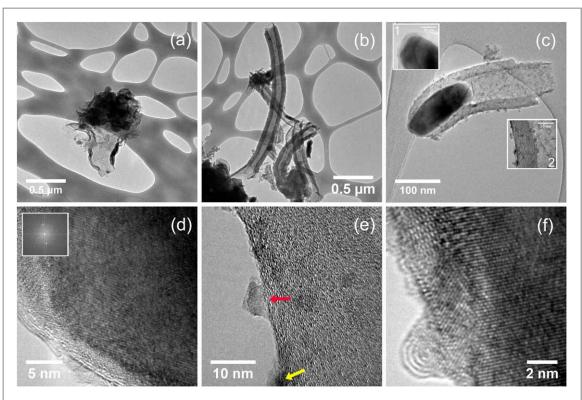
Figure 8. TEM and HRTEM images of CNx-900-SG carbon nanomaterial. Higher synthesis temperature promotes large-diameter CNx-900-SG as are shown in (a). In this image, tangled carbon nanostructures are observed at the tip. (b) Several large-diameter CNx-900-SG. (c) Tip of a broken large-diameter CNx-900-SG containing a nanoparticle (inset 1) and exhibiting a decorated surface (inset 2). (d) The HRTEM image of a catalytic α-Fe, the inset is its FFT image, the zone-axis is [−110], a SAED analysis is shown in figure S15. (e) Small nanomaterial attached to the surface of CNx-900-SG. (f) Fullerene-like carbon nanostructure grown on the α-Fe nanoparticle with [011] zone-axis (see figure S16).

Figure 8(a) displays an unzipping CNx-900-SG probably open due to the robust sonication process with the ultrasonic tip. This carbon nanomaterial exhibits a complicated structure with entangled carbon (probably CNT) at the end. Figure 8(b) shows another group of CNx-900-SG presenting thick walls (~50 nm) and open tips. Interestingly, this CNx-900-SG is decorated with small (~5.3 nm) nanomaterial (figure 8(c)). In inset 1 and inset 2, this type of decoration is observed at the tip or in the lateral surface of CNx-900-SG, respectively. Also, in inset 1 can be seen that the big nanoparticle is surrounded by a thin film of another material different than carbon. This catalyst nanoparticle (figure 8(d)) is monocrystalline α-Fe with a [-110] zone-axis as observed by FFT (see inset figures 8(d) and S15). In figure 8(e) are shown two types of such anchored nanomaterial, one it seems different than carbon with polygonal morphologies (red arrow) and another probably carbon nanomaterial (yellow arrow). Figure 8(f) shows a fullerene-type attached to CNx-900-SG with an interlayer distance of *ca.* 3.7 Å. An EDX analysis on the nanoparticle (figure S16(a)) demonstrates that it contains Fe (see figure S16(b)). The Fe_3C nanoparticle showing a [−4–12] zone-axis is exhibited in figure S17.

Figure 9 depicts the effect of adding SiC powder to the slag to grow N-MWCNTs at 800 °C. There are two types of CNTs: one with a large diameter (red arrow) and another with a smaller diameter and a highly curled morphology (figure 9(a)). The morphology does not change when the slag is altered with SiC. It seems that only the diameter distribution changes. Internal nanoparticles of large diameter CNx-800-SiC are Fe_3C or α-Fe. These nanotubes present an internal structure with double or triple wall groups (figure 9(b)). Unusual morphologies can be found, as shown in figure 9(c), where a giant nanotube with an enormous tip compared with the body is exhibited. An EDS analysis performed at the interface between carbon and a catalytic nanoparticle (magenta circle in figure S18(a)) shows Fe and oxygen content. The oxygen comes from the thin iron oxide film formed around the Fe nanoparticle [80]. Also, copper (from the grid), silicon, and carbon were detected in this CNx-800-SiC. In figure S18(b), the EDS analysis taken at the green circle on the center of nanoparticle shows the presence of O and Fe. Notice that the oxygen signal is smaller concerning to Fe signal. The CNx-800-SiC exhibited in figure 9(d) could be a distinctive nanomaterial found in this sample and not in other cases. The external diameter is approximately 150 nm and a multiwall thickness of around 75 carbon layers. These kinds of CNTs could have a better contribution to high oxygen reduction reaction activity [81]. They also have large inner diameters. Eswaramoorthi and Hwang *et al* [82] fabricated CNTs with large diameters but using anodic titanium oxide. Slag has a diopside containing titanium that could be the causing of such
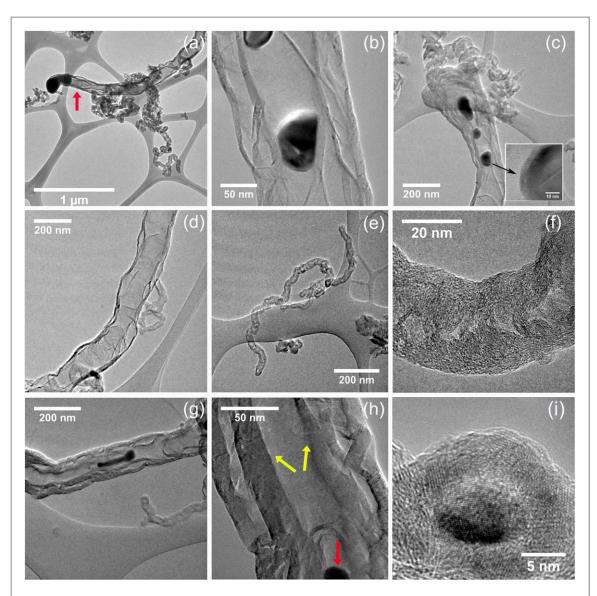
Figure 9. TEM and HRTEM images exhibiting diverse morphology aspects of CNx-800-SiC nanostructures. (a) A giant CNx-800-SiC nanotube of large diameter where small CNx-800-SiC are entangled on it. (b) A section of giant CNx-800-SiC, where two groups of multiwall are appreciable; also, a ~100 nm nanoparticle is encapsulated in the internal cavity. (c) Tip of CNx-800-SiC observed in (b); notice a larger diameter and the presence of tangled carbon nanostructures. (d) The central section of the CNx-800-SiC showed in (b) and (c) exhibiting a large relation between internal diameter (ID) and outer diameter (OD). (e) A small diameter curved CNx-800-SiC nanotube. (f) section of CNx-800-SiC showed in (e) that is similar to CNx-800-SG (figure 6(e)). (g) Giant CNx-800-SiC with a large internal nanoparticle; this enormous CNx-800-SiC presents the double-shell multiwall morphology. (h) HRTEM of (g) where it easy to see the double-shell multiwall with no uniform growing. (i) core–shell material where the core is α-Fe nanoparticle with a [311] zone-axis (figure S19) and the shell is SiO_2 (see figure S20).

structures, but it is necessary to deepen the investigation to clarify such a phenomenon. Unlike those manufactured by Eswaramoorthi and Hwang [82, 83], our CNx-800-SiC nanotubes have internal structures, probably due to nitrogen. CNTs with huge diameters (5 μm) have been produced using laser or electric arc techniques [84]. The structure of the small diameter and corrugated CNTs (figure 9(e)) are like the CNx-T-SG cases, namely, disordered compartments along with curly CNT structure (figure 9(f)). Large diameter CNx-800-SiC with two groups of carbon walls, as shown in figure 9(g), is another morphology that has probably never been reported. The mixture of nanoparticles forming the catalyst probably promoted these two groups of multiwall (see figure 9(g)). Figure 9(h) shows more clearly two groups of multiwall morphology, where the internal nanoparticle (red arrow) possibly generated the internal wall (yellow arrows). In this class of nanomaterial, it was found the morphology presented in figure 9(i), which is spherical nanoparticle (α-Fe) surrounded by silicon oxide, forming a core–shell nanostructure. The core nanoparticle is α-Fe with a [311] zone-axis (see figure S19). The shell part is SiO_2 with a [−132] zone-axis, as is showed in figure S20.

Figure 10 shows the TEM and HRTEM images of CNx-850-SiC nanostructures. Figure 10(a) exhibits an agglomerated CNTs. Figure 10(b) shows an individual CNx-850-SiC with an internal nanoparticle ~40 nm at the tip (red arrow). Figure 10(c) shows this type of CNx-850-SiC exhibiting highly curved, rugged surface and
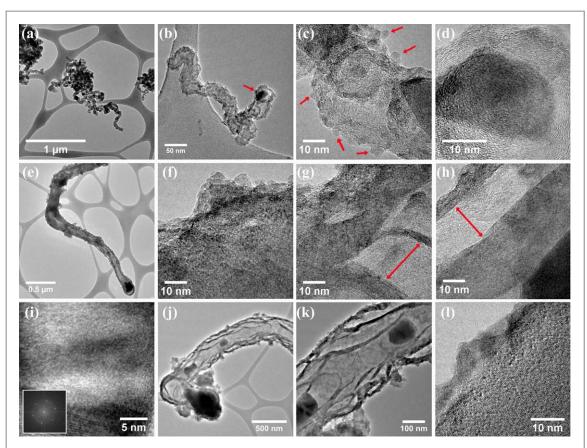
Figure 10. Transmission electron microscopy (TEM) images showing the morphology of the CNx-850-SiC nanostructures obtained using slag + SiC as a catalyst-substrate. (a) Tangled small diameter CNx-850-SiC. (b) A small diameter CNx-850-SiC shows a decorated surface and a catalytic nanoparticle at the tip. (c) The HRTEM image of (b) clearly showing the nanomaterial attached to the surface of CNx-850-SiC. (d) Encapsulated nanoparticle-containing Fe and also some traces of Si (see figure S21). (e) High and non-uniform diameter CNx-850-SiC with surface scab-type nanomaterial. (f) Close view of such scrap-type nanomaterial on the surface of CNx-850-SiC. (g) These nanotubes present the bamboo shape. (h) The HRTEM image of double sets of multiwall morphology. (i) HRTEM of α-Fe nanoparticle with a zone-axis (see figure S22); (j) another giant CNx-850-SiC nanotube with a large diameter (~400 nm). (k) The complicated internal structure of CNx-850-SiC nanotube exhibited in (j). (l) morphology of an individual piece attached to the CNx-850-SiC surface; the composition of such material is showed in figure S23.

~2–3 nm carbon nanoparticles anchored to its surface (red arrows). Notice these CNx-850-SiC present Fe-containing (figure S21) nanoparticles within the cores at the tip (figure 10(d)). Another CNx-850-SiC observed is shown in figure 10(e). This carbon nanostructure consists of a large no-uniform diameter with semi-tubular morphology and nanomaterial with irregular morphology anchored to its surface (figure 10(f)). Analogous to the common N-MWCNTs fabricated with benzylamine and ferrocene [85, 86], they also exhibit a type of bamboo-shape structure with compartments of around 30 nm (see red double arrow in figure 10(g)). Also, there are empty spaces (red double arrow in figure 10(h)) between two carbon groups of walls, which resemble two concentric separated multiwalled-CNTs (figure 10(h)). The phase of the encapsulated nanoparticle in this CNx-850-SiC is α-Fe, as observed in figure 10(i), where FFT analysis (inset) shows the zone-axis of an α-Fe nanoparticle. A more detailed analysis can be consulted in figure S22. Giant tubular carbon structures with large diameters (~400 nm) and several sets of multiwall morphology are also present in this CNx-850-SiC group (figure 10(j)). A big nanoparticle is generating a large diameter, but other internal nanoparticles are also generating the other interior walls. Notice that the compartments are not the typical bamboo shape (figure 10(k)). The attached material on the surface of CNx-850-SiC is also present (figure 10(l)), and according to an EDS analysis, they contain O, Fe, Al, Si, S, (see figure S23(a)). Figure S23(b) shows the EDS analysis of the encapsulated nanoparticle being Fe the main element found.

Different aspects of the carbon nanomaterial obtained from the CNx-900-SiC group are exhibited in figure 11. Clusters of irregular CNT with curling shape are revealed in this sample (figure 11(a)). Large diameter multiple sets of multiwall carbon giant structures were detected in this group of CNT (red arrow in figure 11(b)). The diameters of these CNTs are approximately 300 nm. A huge catalyst nanoparticle with a dimension of 570 nm long and 300 nm of diameter are associated with their synthesis (red squared). Notice the tiny CNT below this giant CNT (green arrow). Graphene-like flakes (blue arrow) and extremely large dimension CNx-900-SiC (yellow square) structures were observed. This image also exhibits a straight CNx-900-SiC nanotube with 80 nm
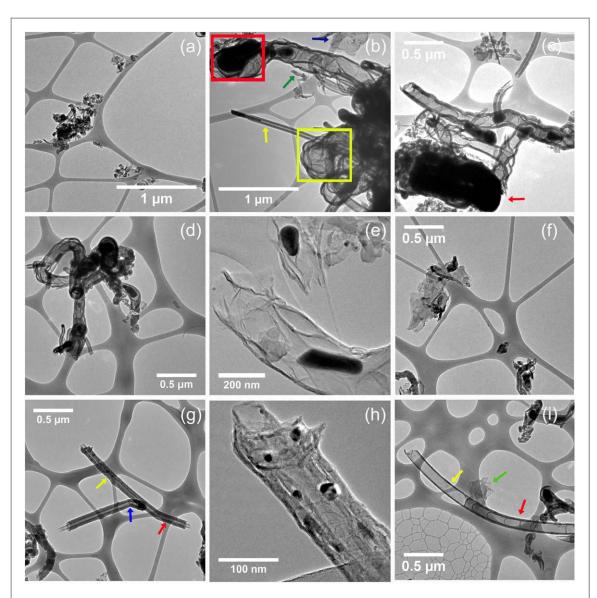
Figure 11. TEM images showing the morphologies of the CNx-900-SiC. (a) Conglomerates of CNx-850-SiC. (b) Giant CNx-900-SiC nanotube associated with an enormous catalytic nanoparticle (~600 nm long), here it is also possible to distinguish giant structures probably being part of a super-huge tangled of diverse carbon structures impossible to analyze by TEM. (c) Other giant CNx-900-SiC nanotubes anchored to a big nanoparticle probably promoted by the SiC powder. (d) Complex multi-nanotubes structure consistent in small and large diameter CNTs. (e) Large diameter CNx-900-SiC presenting few carbon layers. (f) An individual slice is probably coming from a large CNx-900-SiC. (g) Two CNx-900-SiC with an average diameter (~100 nm) that present interesting morphology aspects (see text). (h) The superior part of CNx-900-SiC (yellow arrow) in (g), presenting two or three sets of multiwall where catalytic nanoparticles are probably trapped. (i) Bamboo shape CNx-900-SiC exhibiting two different types of internal morphology.

of diameter (yellow arrow). Figure 11(c) also shows several large diameters (~100 nm) CNx-900-SiC with sizable nanoparticles distributed alongside. Note the massive structure that is accompanying these CNTs (red arrow). Figure 11(d) exhibits the different carbon structures found in the CNx-850-SiC group, namely large-diameter multi-wall, small diameter, and curly CNTs. Another tremendous CNx-900-SiC structure is displayed in figure 11(e). Its diameter is close to 275 nm. These giant carbon structures can be useful to the catalysis process at the nanometric level [82, 83]. Because they have several compartments at the same level could be applied to have molecules with different functional activity. They can be carefully broken to fabricate large graphene sheets using the Elias *et al* method [87]. Figure 11(f) shows graphene-like transparent material identified in this sample, which can indicate that it is a material of a few carbon layers. Another kind of CNTs can be further found, as is showed in figure 11(g). Note as the upper CNx-900-SiC (red arrow) start with a like-normal multiwall morphology with an internal diameter of one-third of external diameter. However, after some distance, a double set of multiwall starts continuing to the end. This last part presents a disordered structure with several internal nanoparticles alongside the walls. Probably their electrical properties are different when the electrons change from one zone to the other. The lower CNx-900-SiC (blue arrow) presents a very pronounced folded close to the tip. Important to mention that the bamboo shape in this kind of carbon structure is not well defined, as can be seen in figure 11(h), which is a magnification of the upper CNx-900-SiC of figure 11(g). Note that the

compartments are irregular and the borders consist of few carbon layers. Figure S24 shows two EDS spectra of colored nanoparticles from figure 11(h), red (a), and green (b). According to these spectra, both nanoparticles contain Fe. Figure 11(i) displays another N-MWCNT from the CNx-900-SiC group presenting a bamboo shape of a large diameter. However, their compartments are not uniform and suddenly stop appearing (see red arrow). Besides, graphene-like structures could be detected in this TEM image.

3.3. XRD characterizations

Figure 12 shows the x-ray diffractograms for all the samples obtained from the different synthesis conditions. Figure 12(a) presents CNx-800 (red), CNx-800-SG (blue) and CNx-800-SiC (black) cases. Fe_3C (asterisks) and C (rhombs) are clearly identifiable. In CNx-800-Sg also there is a peak associated with β-SiO_2 (star) and in both CNx-800-SG and CNx-800-SiC α-Fe phase (inverse filled black triangles) is present. There is a broad peak observed between 10–15 2θ-degrees, which is likely due to the presence of intercalated graphite oxide. Figure 12(b) corresponds to the 850 °C temperature synthesis cases. CNx-850 presents a shoulder at around 21 2θ-degrees correlated to β-SiO_2. In this sample, the Fe_3C peaks (asterisks) were not resolved. The only difference between CNx-800-SG (CNx-800-SiC) and CNx-850-SG (CNx-850-SiC) was the existence of a peak at 24 degrees related to the expanded graphite (EG). This situation could be related to the phenomenon observed in figure S17, where the significant distance between carbon layers where observed When the N-MWCNTs are synthesized at 900 °C the β-SiO_2 and EG phases are not present (figure 12(c)). The SiC phase was not detected in any CNx-T-SiC (T = 800 °C, 850 °C, and 900 °C).

3.4. Raman characterization

Figure 13 depicts the Raman spectra for the N-MWCNTs obtained at 800 °C (figure 13(a)), 850 °C (figure 13(b)), and 900 °C (figure 13(c)). CNx-800 (red curve in figure 13(a)) presents an I_D/I_G = 1.14, probably associated with the rugged surfaces of this sample. The I_D/I_G for CNx-800-SG (blue curve in figure 13(a)) is 0.83, which is associated with the purity of CNT or low degree of disorder in CNT [88]. According to SEM and TEM characterization of this CNx-800-SG, they show a dramatic curved structure with some defective surface and complicated internal morphology. However, HRTEM shows that even such accidental and irregular framework of such CNT, these are formed with well-defined graphitic layers. The I_D/I_G for CNx-800-SiC (black curve in figure 13(a)) is 0.89, a close value to the CNx-800-SG case. Due to the morphologies of CNx-800-SiC and CNx-800-SG are very similar, probably this increase in I_D/I_G for CNx-800-SiC could be associated with the small nanoparticles attached to the CNx-800-SiC surfaces (figure 6(e)). The Raman spectra of N-MWCNTs for the three cases studied at 850 °C synthesis temperature (figure 13(b)) exhibit a comparable behavior with the 800 °C case. The value of I_D/I_G for CNx-850 is 1.28, being larger than the CNx-800 case. According to figure 3(d), these CNT present larger diameters and rougher surfaces, also there are more entangled small diameters CNx-850, which could be associated with this increase. CNx-850-SG (blue curve) presented I_D/I_G = 0.81 very similar than CNx-850. Also, the values of I_D/I_G for CNx-850-SiC do not differ from CNx-800-SiC being, in this case, 0.82. CNx-900-SG and CNx-900-SiC exhibit ID/IG values of 0.83 and 0.96, respectively. In these two latter cases, the structures showed in figure 11(d) (yellow squared) possible are to attribute for the increase in I_D/I_G in the case of CNx-900-SiC.

3.5. XPS characterization

Different chemical functional groups attached to the surface or edges of N-MWCNTs were analyzed by x-ray photoelectron spectroscopy (XPS). According to these results, the total atomic concentrations of carbon, nitrogen, oxygen, and silicon depend on the synthesis temperature and the type of CNx (see table 2).

Due to the chemical characteristics of samples, when the XPS is performed in CNx-T-SG or CNx-T-SiC (T = 800 °C, 850 °C, and 900 °C), the surveys present several peaks that were not considered for simplicity of analysis. We only present the results were carbon, nitrogen, oxygen, and silicon are involved. For instance, CNx-800 presents a concentration of carbon, nitrogen, oxygen, and silicon of 64.3 at%, 2.0 at%, and 22.6 at%, and 8.9 at%, respectively. However, CNx-800-SG and CNx-800-SiC contain more than 76 at% of C1s, which is around 15% more than the CNx-800 case. This situation is inverse when the synthesis temperature is increased to 850 °C where the C1s concentration in CNx-850 is the highest (77.1%) comparing with CNx-850-SG (64.1%) and CNx-850-SiC (75.8%). The previous situation is repeated for CNx-900 and CNx-900-SG, where C1s concentration is 78.8% and 61.0%, respectively. However, in the case of CNx-900-SiC, the C1s concentration increase to 84.1 being the highest. In the case of N1s, the concentration oscillates between 1.3% (CNx-850-SG) and 3.6% (CNx-900-SiC). This last feature could be the cause of morphologies, as presented in figure 11(b). When slag is mixed with SiC, the N1s contain is relatively high of 2.4% in CNx-800-SiC, 1.8% in CNx-850-SiC, and 3.6% CNx-900-SiC. However, the lowest values over the N1s average are for CNx-T-SG, where T = 800 is 1.7%, T = 850 is 1.3%, and T = 900 is 2.2%. Really large values of O1s were found in most of the cases being the
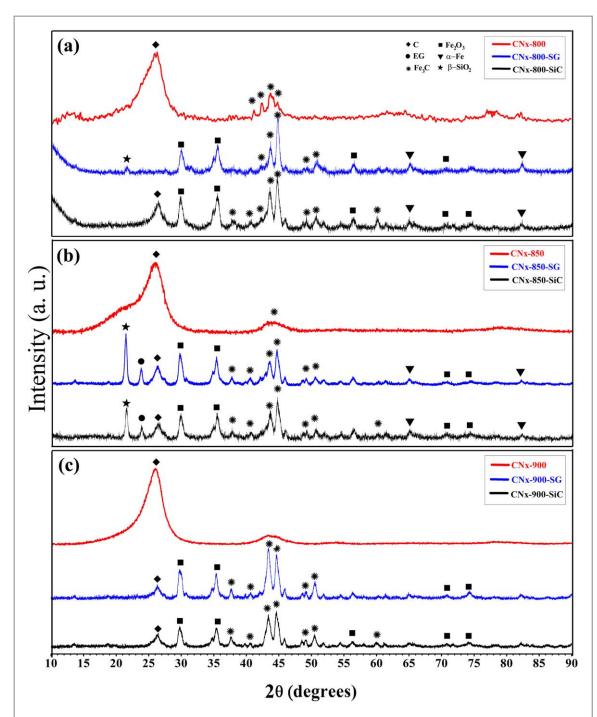
Figure 12. x-ray diffraction (XRD) patterns of N-MWCNTs synthesized at 800 (a), 850 (b) and 900 °C (c) using ball-milled slag (red XRD), SG-2h (blue XRD), and SG-SiC (black XRD) as a catalyst. The presence of Fe_3C (asterisks) is clearly in all of the cases identified, but not for CNx-850 and CNx-900. The broad peak observed between 10–15 2θ-degrees in some samples is likely due to the presence of intercalated graphite oxide. The presence of β-SiO_2 (stars) is clearly observed in CNx-850-SG and CNx-850-SiC. In addition, a peak of expanded graphite (EG) is detected in both samples (bullet black). The peaks with inversed triangles corresponding to α-Fe. Magnetite crystalline phase is denoted with a filled black square.

highest for CNx-850-SG (26.7%) and the lowest for CNx-900-SiC (10.4%). SG-2h in benzylamine provokes high O1s to contain in N-MWCNTs which could be very important to electrochemistry studies [89]. This phenomenon has been studied, and it is attributed to the possible oxidation of benzylamine [90, 91]. At higher temperatures, this process is less than possible. Contrary, in the case of CNx-900-SG, the XPS results show an increasing of O1s concentration with the temperature. Here the oxygen might come from the metal oxides that are not in the CNT, probably due iron oxide (Fe_3O_4). From the SEM and TEM result, it was possible to observe that CNx-850-SG are attached to large nanoparticles formed by similar elements than the original slag. At higher temperatures, these nanoparticles are more prone to accept oxygen atoms. Although in the case of SiC is added to slag also CNx-T-SiC attached to large nanoparticles are observed, the cases of CNx-T-SiC have completely different behavior than CNx-T-SG. Also, slag in some cases foments concentration of Si2p since 1.2% in the
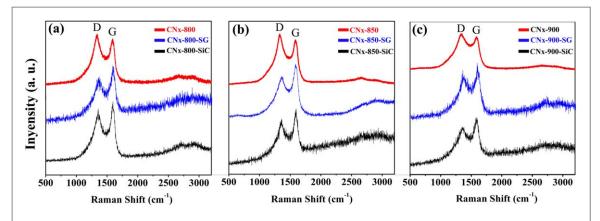
Figure 13. Raman spectra of N-MWCNTs synthesized at 800 (a), 850 (b), and 900 °C (c) using a 514 nm excitation laser line. The corresponding I_D/I_G ratios are given in the text. The red, blue, and black Raman spectra correspond to CNx-T, CNX-T-SG and CNx-T-SiC cases, respectively.

Table 2. Atomic concentrations derived from XPS characterizations for CNx produced at different temperatures and using different synthesis procedures.

	Atomic concentration (%) in N-MWCNTs								
Element									
Sample	CNx-800	CNx-800-SG	CNx-800-SiC	CNx-850	CNx-850-SG	CNx-850-SiC	CNx-900	CNx-900-SG	CNx-900-SiC
C 1s	64.3	78.9	76.4	77.1	64.1	75.8	78.8	61.0	84.1
N 1s	2.0	1.7	2.4	1.6	1.3	1.8	3.1	2.2	3.6
O 1s	22.6	17.7	17.5	15.3	29.0	17.6	11.3	26.8	10.4
Si2p	11.1	1.7	3.7	5.9	2.6	4.7	6.8	10.1	1.2

CNx-900-SiC case to high as 11.1% or 10.1% for CNx-800 and CNx-900-SG, respectively. It has been reported nanostructured Si for high energy lithium-ion batteries due to it has ten times higher specific capacity than traditional carbon anodes [92]. The percentage of Si2p considerably decreases in CNx-T as T increase from T = 800 °C (11.1%) to T = 850 °C (5.9%), then at 900 °C (6.1%) remains approximately constant. Contrary to the previous case, CNx-T-SG increases the content of Si2p as the synthesis temperature raises. For example, for CNx-800-SG Si2p is 1.7%, for CNx-850-SG is 2.6% and for CNx-900-SG is 10.1%. The content of Si is probably associated with the encapsulated or attached nanoparticles, which were detected by EDS in these samples. It is very probable that also the change of morphology exhibited in figures 6, 7 and 8 are related to the interaction between Si, N, and Fe in the CNT growth process. When additional SiC is involved in the catalyst for CNx fabrication the Si2p % content, also increase from 3.7% in CNx-800-SiC to 4.7% in CNx-850-SiC. The decrease of Si2p in CNx-900-SiC could be correlated with the increase in temperature where possible SiC is sublimated. Therefore, SiO_2 is the main Si-nanomaterial that could interact with C, N, and Fe. SiO_2 nanomaterials were found at the shell of Fe, or Fe3C encapsulated nanoparticles (figures S9 and S20).

3.5.1. High-resolution XPS

Results on the deconvoluted spectrum are summarized in table S1 (supplemetary information). For the C1s signal, all samples revealed the presence of sp^2 (C=C) and sp^3 (C–) hybridizations with binding energies of ~284 eV and ~285.2 eV, respectively. Trace of C-O (phenolic) and O–C=O (carboxyl) bonds were also detected with binding energies around 286 eV and 288 eV. For N1s spectra, we analyzed the N-pyridine, N-pyrrolic, N-graphite or quaternary, and N–O bonds in the carbon materials. The deconvolution of the O1s signal defined four main contributions. The lowest energy corresponds to metal oxides functionality at around 531 eV, in this case, the oxygen contribution could be C=O (carbonyl) due to the formation of quinones, the C–O and the O=C–O functionalities part of the ester, anhydrides and the formation of phenolic groups are located around 532–533 eV. The ether functionality (C–O–C) is located about 533 eV (533.1–533.8), and the oxygen atom in the carboxyl groups (-COOH) is around 534.5 eV. In the case of Si2p, four main contributions were de-convoluted from each high-resolution spectrum, namely, SiC, SiC-β, Si_2O_3/SiC, and SiO_2. The only case where siloxane was detected was CNx-800.
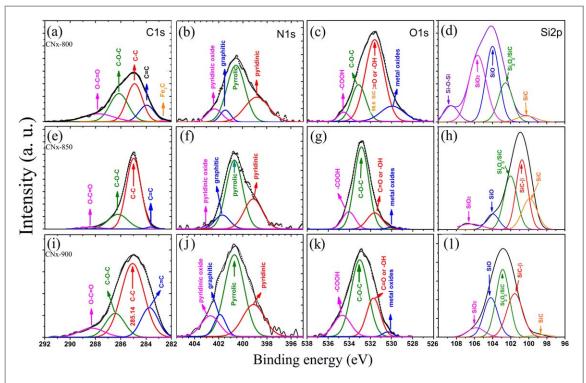
Figure 14. x-ray photoelectron spectroscopy (XPS) analysis for N-MWCNTs synthesized at 800 °C (a)–(d), 850 °C (e)–(h), and 900 (i)–(l) C1s (a), (e) and (i), N1s (b), (f), and (j), O1s (c), (g) and (k), and Si2p (d), (h) and (l) line scan are shown. All peaks were deconvoluted and assigned to different chemical species. All N-MWCNTs were grown using slag as the catalytic source.

3.5.1.1. CNx-T cases (T = 800, 850 and 900 °C)

According to the C1s spectrum, there is a large amount of sp^3 hybridized carbons revealed by the XPS characterization for the three synthesis temperatures studied (figures 14(a), (d), and (g)), which agrees to the Raman characterization where all these samples presented low quality of graphitization. Interesting is that the number of C–O–C functionalities is considerably large, which are related to the ether group (ethoxy, methoxy, or epoxy) generally formed in defective surfaces or edges of carbon nanomaterials [93].

The bind of C with metals is only manifest in Fe$_3$C at 282.6 eV for the CNx-800 case. N1s spectrum of CNx-800 indicates the presence of pyridinic nitrogen at 398.89 eV, pyrrolic nitrogen at 400.58 eV, and graphitic nitrogen at 401.4 eV. The pyridinic oxide nitrogen is also found at 402.3 eV (see figure 14(b)). CNx-850 yielded the following binding energies: pyridinic 399.12 eV, pyrrolic 400.68 eV, graphitic 401.86 eV, and pyridinic oxide at 403 eV. The percentage of this latter type of nitrogen is considerably reduced. We found the same four types of nitrogen defects with slightly different binding energies for synthesis at 900 °C (figure 14(j)). In general, all samples shown high concentrations of N-pyrrolic, which is not common in a conventional synthesis of N-MWCNTs [94]. It is notable that in all the cases, pyrrolic N is the most abundant functionality in CNx-T (around 50%). This situation could be correlated with the increase of disorder and the presence of SiC in the sample. It seems that pyrrolic functionality is correlated with the corrugated surface and large diameter of the CNx-T cases. This situation could be attributed to silicon carbide material contained in the original slag (see figure S4), note that a relatively large concentration of Si was detected in the slag material (around 15.4%). Therefore, Si atoms could act as anchor points for the nitrogen-atoms, as experimental reports have demonstrated that the SiC surface favored the formation of pyrrolyl groups due to the Si-N linkage [95, 96]. The high-resolution O1s spectrum of CNx-800 presents a significant contribution from carbonyl carbons or hydroxyl groups. There is a relatively substantial contribution from metal oxides, which is concordant with the x-ray results. This type of bond considerably diminished in CNx-850 and CNx-900 (see figures 14(g) and (k)). The ether functionalities increase their percentage and decrease the carbonyl functional groups or phenolic functional groups contribution also for CNx-850 and CNx-900 (see table S1). It is characteristic in all synthesis temperatures that the morphologies of CNT are complex with junctions and curved shapes. Deconvolution of high-resolution XPS Si2p spectrum exhibits in CNx-800 the signal of siloxane (Si–O–Si) accompanied by a large percentage of SiO$_2$ and SiOx together with signals of following other chemical states Si$_2$O$_2$/SiC and SiC (figure 14(d)). In the case of CNx-850, the reduction of both SiO$_2$ and SiOx is evident, and the siloxane group is not present anymore. Now the most important bands are related to the interaction between SiC and Si$_2$O$_2$ and the SiC itself. For CNx-900, the signal of SiC almost disappears being the most crucial SiO$_2$/SiC signal (figure 14(l)).
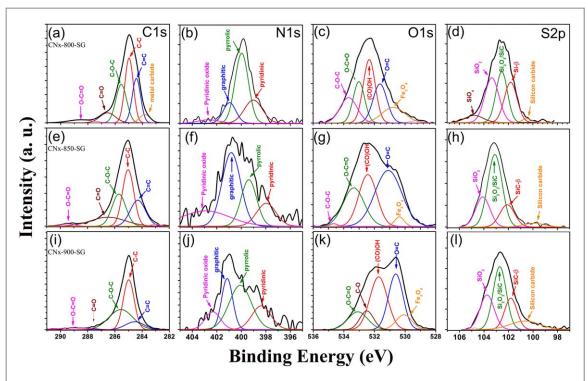
Figure 15. x-ray photoelectron spectroscopy (XPS) analysis for CNx-T-SG synthesized at 800 °C (a)–(d), 850 °C (e)–(h), and 900 °C (i)–(l); C1s (a), (e) and (i), N1s (b), (f), and (j) and O1s (c), (g), and (k) and Si2p (d), (h) and (l) high-resolution line scan are shown. All peaks were deconvoluted and assigned to different chemical species. All N-MWCNTs were grown using slag as a substrate containing catalytic material.

3.5.1.2. CNx-T-SG cases (T = 800, 850, and 900 °C)

XPS results for CNx-T-SG samples are presented in figure 15. In all three the cases considered, C1s spectra revealed the presence of sp^2 (C=C) and sp^3 (C-C) hybridizations with binding energies of ~284 and ~285 eV, respectively. Besides, metal carbide is present but only in the CNx-800-SG case. Phenolic, carbonyl, and carboxyls are also present at ~286 eV, ~287 eV, and 288 eV.

C1s spectra for CNx-850 and CNx-900 (figures 15(e) and (i)) are very similar, with slightly contribution differences for the distinct functional carbon groups. In these two latter cases, there was not detected metal carbide. Although the contribution of sp^3 is still significant here for all CNx-T-SG (T = 800 °C, 850 °C, and 900 °C), the C=C also is important. For N1s spectra, N-pyridine, N-pyrrolic, N-graphite or quaternary, and N-O bonds in this carbon material were observed (figures 15(b), (f), and (j)). Like the CNx-T case, here, high concentrations of N-pyrrolic are one of the most important hybridizations. Graphitic N is also abundant in the CNx-850-SG and CNx-900-SG cases at the expense of the decrease of N-pyrrolic as can be seen in figures 15(f) and (j). These results are concomitant with Raman spectroscopies issues (see figure 13(b)). From O1s, high-resolution signals can be constructed five main contributions. At around 531 eV, the contribution could be attributed to magnetite (Fe$_3$O$_4$) that was detected by x-ray characterization. At around 531 eV and 532 eV, the oxygen contribution can be associated with C=O (carbonyls) and ester (COO–), respectively. C–O–C ether (~533 eV) and –COOH (oxygen in carboxyl groups) is around 534 eV. In this case, CNx-800-SG presents an appreciable amount of oxygen in carboxyl groups (-COOH), which is not in CNx-850-SG and CNx-900-SG. This functionality increases the acidic behavior of the sample and their potential to be used in the adsorption of positive ions for Li-ion rechargeable batteries [97] and metallic contaminants removal [98]. Also, –COOH functionality helps in the formation of linking amine-carboxylic bonds to incorporate polymeric structures to create cross-linked CNT structures [99] and the functionalization with enzymes [100]. However, there is a Si2p detectable contribution to the survey spectrum of CNx-T-SG samples (see figures 15(d), (h), and (l)). Silicon carbide (~100 eV) or SiC-β (~101 eV) were identified. Also, oxides alone (SiOx) and oxides interacting with SiC as Si2O3/SiC at ~104 eV and ~103 eV were revealed (see figures 15(d), (h), and (l)). In CNx-850-SG and CNx-900-SG, the interaction between Si$_2$O$_3$ and SiC is more significant, as can be appreciated in figures 15(h) and (l).

3.5.1.3. CNx-T-SiC cases (T = 800, 850 and 900 °C)

Figure 16 shows the deconvolutions obtained from the high-resolution XPS of C1s (first column), N1s (second column), O1s (third column), and Si2p (fourth column). C1s spectra consist of four contributions, namely, the presence of sp^2 (C=C) and mostly sp^3 hybridizations (C–C) at ~284 and ~285.2 eV, respectively. Notice that the
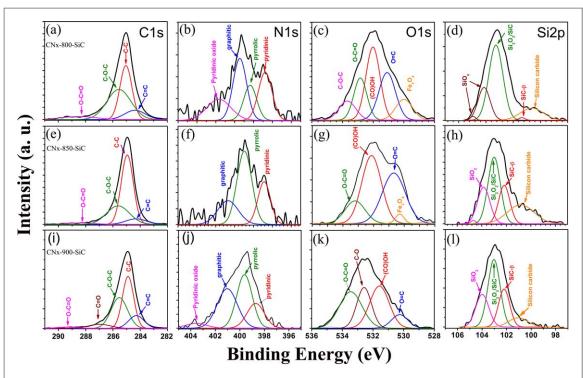
Figure 16. x-ray photoelectron spectroscopy (XPS) analysis for CNx-TEMP-SiC synthesized at 800 °C (a)–(d), 850 °C (e)–(h), and 900 (i)–(l); C1s (a), (e) and (i), N1s (b), (f), and (j) and O1s (c), (g), and (k) and Si2p (d), (h) and (i) high-resolution line scan are shown. All peaks were deconvoluted and assigned to different chemical species. All N-MWCNTs were grown using a powder of slag mixed with SiC as a substrate containing catalytic material.

sp^2 hybridization is decreasing as temperature increase from 800 °C to 850 °C (see figures 16(a), (e)), then slightly increase to CNx-900-SiC (figure 16(i)). Also, the ether functionalization (C–O–C) present the same behavior. This behavior could be associated with the morphology observed in figures 9, 10, and 11, where some carbon nanostructures showed no regular shape (figures 9(c), 10(a), (b), (e), and 11(b), (c)). In the case of N1s, in CNx-800-SiC N-graphitic atoms present a significant contribution to the high-resolution spectrum than N-pyrrolic or N-pyridinic (figure 16(b)). There are more N-pyridinic than the component of N-pyrrolic. The high-resolution N1s spectrum of CNx-850-SiC is different from the CNx-800-SiC case. Here the concentration of N-pyrrolic is the highest, followed by N-pyridinic and then N-graphitic. Synthesis of N-MWCNTs carried out at 900 °C does not appreciably change the concentration of N-pyrrolic but modify the concentration of N-graphitic being now the second-largest concentration that appears in the high-resolution N1s spectrum (see figure 16(j)). The O1s signal for CNx-800-SiC consists of five contributions. The lowest energy corresponds to metallic oxides (Fe$_3$O$_4$) at ~530 eV, O=C at ~531 eV (carbonyls) followed for COO– corresponding to ester, amides, and anhydrides at ~532 eV, then C–O–C about ether group at 533–534 eV and finally COOH which is the carboxylic family at 534 eV. In the case of CNx-850-SiC, this situation changes because now only four chemical species were deconvoluted mainly, namely Fe$_3$O$_4$, O=C, COO– and C–O–C, no deconvolution of COOH was possibly found. Probably due to the temperature, this chemical group was not formed at the CNT surface. CNx-800-SiC show a Si2p contribution by five chemical bindings (see figures 16(d), (h), and (l)), specifically SiOx (minimal contribution) at ~105 eV, SiO$_2$ at ~104 eV, Si$_2$O$_3$/SiC at ~103 eV, SiC-β (minimal contribution) at ~102 eV and SiC at 101 eV. In CNx-850-SiC and CNx-900-SiC, the panorama change for SiC-β, which considerably augments probably due to the increase of temperature. These high resolutions XPS for CN$_X$-T-SiC demonstrate that SiC global participation in the Si2p spectrum (Si$_2$O$_3$/SiC, SiC-β, and SiC components) is considerably larger than in CNx-T-SG.

3.6. TGA results

TGA curves for different N-MWCNTs studied here are shown in figure 17. From 50 °C to 100 °C all the samples lost material, probably corresponding to water evaporation or released of other attached molecules [101, 102]. In the case, CNx-800 (black curve in figure 17(a)) reveals a weight loss of ~40% at 900 °C in oxygen atmosphere with two significant temperatures of oxidation (TO) present one at ~300 °C probably corresponding to amorphous carbon [29] and the other at ~490 °C corresponding to the CNx-800. In the CNx-800-SG (red curve in figure 17(a)) case, the loss of amorphous carbon (~20%) is considerably smaller than the CNx-800 case. At ~475 °C this sample loss ~60% of its weight corresponding to the CNx-800-SG. CNx-800-SiC (blue curve in
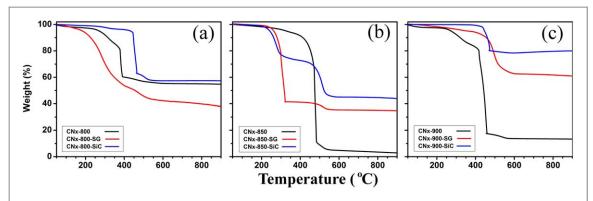
Figure 17. TGA curves corresponding to CNx-T (red curves), CNx-T-SG (blue curves), and CNx-T-SiC (black curves) synthesized at different temperatures (a) 800 °C; (b) 850 °C, and (c) 900 °C. It is notable the significant amount of residual material when the slag is used as a catalytic substrate (blue and black curves). If the slag is used as a catalytic source, the residual material is considerably reduced, except in the 800 °C case, see (a). This phenomenon could be because not all Fe included in the slag is not used in the synthesis because the temperature was not appropriated to synthesize them.

figure 17(a)) loss only 40% of its weight at 900 °C and the TO in this interval is at 448 °C. Synthesis at 850 °C produced CNx type with relatively different thermal stability in an oxidizing atmosphere, as can be seen in figure 17(b). CNx-850 (black curve) exhibits a typical behavior of doped CNTs [25]. The TO for CNx-850 is 481 °C which is higher than reported by Cruz-Silva, *et al* for similar doped carbon nanotubes [25]. There is another TO for CNx-850 at 473 °C probably associated with the other CNx-850 with smaller diameter, because these CNTs present a bimodal behavior for diameter distribution. It is probably that each diameter is related to each oxidation temperature. The remnant material is only ~3%, which means that ~88% correspond to CNx-850 nanotubes. The thermal stability of the CNx-850-SG (red curve in figure 17(b)) reach to 250 °C with the first TO of ~300 °C, where probably amorphous or turbostratic carbon is oxidized [29]. The second interval of thermal stability (approximately 160 °C) from 320 °C to 480 °C is observed then 5% of the mass is consumed. Around 35% is probably converted into oxides. The second TMO ~515 °C could be correlated with the CNx-850-SG showed in figure 7(c). Similar behavior is found for CNx-850-SiC sample (blue curve in figure 17(b)), but only two oxidation temperatures were noticed (see figure 17(b)), one at 276 °C (functional groups and amorphous carbon) with a related mass loss of 23%. This sample was instable during 140 °C, where mass was consumed gradually. The sample was not oxidized from ~570 °C to 900 °C. The TO is ~514 °C which could associate with the same type of CNTs. These two last results are concomitant with the Raman spectra associated with these samples. Although the carbon structures like presented in figures 7(b), (c), 10(b), and (c) are curved, they exhibit well-ordered carbon layers that could be responsible for the larger TOs observed. The TGA results of samples synthetized at 900 are presented in figure 17(c). The sample CNx-900 (black curve) exhibits 3 TO (~420 °C, ~453 °C, and 460 °C). In the first 100 °C, the sample loss very few mass (~3%). Then the mass was gradually decreased during the scan from ~ 170 °C to 412 °C. An abrupt mass was consumed (~65%) in an interval of 45 °C. During ~125 °C the mass has a linear diminution of 5% being the residual mass 12%. According to the Raman results, the crystallinity of this sample is no good, which is related to the result of the largest TOM found (~460 °C) to this sample. However, the CNx-900-SG (red curve in figure 17(c)) and CNx-900-SiC (blue curve in figure 17(c)) present a considerable residual mass of 60% and 80%, respectively. Above 450 °C, these two samples also exhibit TOMs of 493 °C and 472 °C, respectively. These results are concomitant with the Raman spectroscopy I_D/I_G values. The reason for such results is that CNx-900-SG and CNx-900-SiC are firmly attached to the catalyst nanoparticles (see figure 11(c)) from which they are growing. Notice that CNx-900-SiC is increasing its weight after 600 °C. CNx-900-SiC also presented two oxidation temperatures (441 °C and 471 °C) again, possibly associated with the two kinds of CNTs observed: one with a large diameter (figure 11(b)) and the other with curved morphology (figure 11(a)).

To clarify the TGA results of all CNx studied. We also performed TGA of 'pure' slag, 2h ball-milled slag, 2h ball-milled (slag + SiC), and only SiC used in the fabrication of different CNx samples. The results are shown in figure 18. Around 400 °C 'pure' slag starts to oxidize, increasing its weight (red curve) being more than 2% of its initial weight at 950 °C. Probably oxygen is incorporating with the temperature to the slag sample by oxidation of Fe, Si, Mo, and probably aluminum compounds. In the case of a 2h-milled slag (blue curve), the TGA curve starts to slowly decrease approximately at 80 °C losing 1% of its weight due to mainly water evaporation, then at ~300 °C the weight increases almost linearly gaining 7% of its initial weight. Here the size reduction is fundamental for the oxidation process to increase the weight. Due to this size reduction, the reactivity of this sample has been augmented. When SiC is added to the slag, and the resultant sample is milled for 2h, the specimen presents a strange behavior when it is oxidizing. Instead of reducing its weight, this is also increased
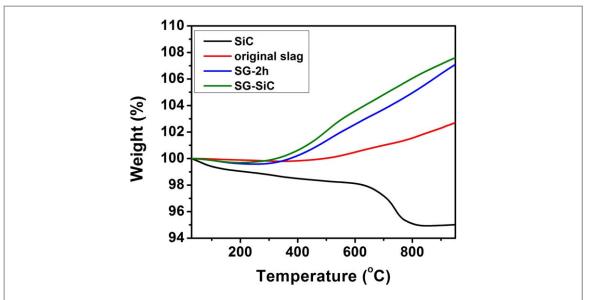
Figure 18. TGA curves of (1) SiC used to prepare the catalytic substrate for CNx-TEMP-SiC carbon nanostructures (black curve); (2) pure mine tailings before ball milling process (figure SI2b, red curve); 2 h ball-milled mine tailings (blue curve) and 2 h ball-milled mine tailings mixed with SiC powder (green curve).

more than the precedent sample reaching 950 °C to 7.5% more weight than its initial mass. The reason for such behavior could be related to the size of SiC is considerably affected by the milling [107]. For SiC, the TGA curve (black) is monotonically reduced almost linearly until ∼620 °C where a relatively large amount of loss weight happens, reaching ∼95% at 820 °C. At the first 200 °C, the reducing of mass must be because of the water evaporation [103]. The following 400 °C, the mass loss could be associated with functional groups added to the SiC nanoparticle surface. A mass reduction of 3% happens between 600 °C and 800 °C related to the carbon oxidation [102]. After 800 °C starts the formation of a thin film of silicon oxide [104] and the mass is increased.

3.7. Discussion

One of the main substances used in this CNT synthesis is the benzylamine ($C_6H_5CH_2NH_2$), which is an organic chemical compound that is a source of NH_2. When CNx-T (T = 800 °C, 850 °C, and 900 °C) is fabricated, the benzylamine is strongly affected because it interacts with the elements contained within the slag. It seems that the iron carbonyl sulfide acts on the benzylamine because it turns green with time. According to XPS results, all the sample CNx-800 contains high amounts of O1s (24.4%). This iron carbonyl sulfide could be the source of such oxygen in the solution, although also diopside or pyroxene could participate as oxygen sources. In the case of CNx-850 or CNx-900, the O1s were reduced (16.5% and 11.7%, respectively). Here the synthesis temperature plays an essential role in the decrease of this oxygen concentration in the samples. In consonance with SEM and TEM results the three kind CNx-T nanotubes present two diameters. Also, the CNx-T nanotubes with a large diameter exhibit small internal diameter. It is probably that oxygen participates actively in the formation of such CNTs as when ethanol is used. It is essential to mention that the CNx-T-SG and CNx-T-SiC samples are composed of substrate and carbon nanotubes (see TGA results). In the case of CNx-T-SG, the results are entirely different from the CNx-T. For instance, in CNx-T-SG group, the O1s concentration increases with synthesis temperature from 17.7% to 29.9% and then 41.6% to 800 °C, 850 °C, and 900 °C, respectively. Figures 3(b), (e), and (h) show the CNx-T-SG attached to particles of material that probably contain similar material than the original slag. With the increasing synthesis temperature, these nanoparticles possibly grow due to coalescence. It is probably that some percentage of such substrate participate as a source of oxygen and an increase of O1s concentration. When SiC is mixed with the slag to be used as a substrate for N-MWCNTs fabrication, O1s content of samples CNx-800-SiC and CNx-850-SiC are similar than the CNx-800-T and CNx-850-T cases. However, at 900 °C, the situation changes because at the surface of SiC nanoparticles probably starts to grow a SiO_2 thin film. Therefore, it is easier to pull apart the carbon nanotubes from the substrate and some parts of the O1s concentration decrease could come from there.

A possible scenario for the mechanism formation of the morphologies here presented is as following. In the case of CNx-T, the slag is transported from the sprayer vessel by Ar-H_2 together with benzylamine and deposited on the quartz tube. Then occurs the formation of Fe clusters impelled by the hydrogen starts. However, a lot of oxygen is participating in the process of synthesis, and the carbon layers are not well-formed. Although the growth is faster than usual and carbon layers grow more rapidly with the increase of temperature, the crystalline

grade of these CNT is affected as SEM and TEM images illustrated. Also, sulfur is acting all the time, forming Y and kink structures at higher temperatures [31]. This situation provokes the growth of carbon nanostructures with large diameters and disorder in the layers, inclusive of the generation of coaxial morphologies. The superficial corrugated structure of these samples could be related to the intervention of SiC contained in the slag. The situation is different in the case of substrates are SG or SG-SiC. In these cases, first, the hydrogen starts to reduce and morphologically change the Fe_2O_3 nanoparticles on the slag resulting in Fe_3C or Fe catalytic nanoparticles [105]. The slag is also interacting with the quartz tube. Inclusive SiC is also interacting with quartz since the beginning of synthesis. In this situation, small Fe-containing nanoparticles begin to catalyze carbon nanotubes like those in figures 6(d), 7(b), 9(e), and 10(b) with exaggerated curved morphology and rugged surface. However, the Fe-containing nanoparticles continue coalescing, and big nanoparticles can be formed [106]. The formation of long and irregular nanoparticles is typical when the amount of catalyst source is few. This kind of giant catalyst nanoparticles promotes the formation of giant nanotubes with an irregular internal structure and two or more sets of multiwall as figure 9(b). The participation of SiC is crucial as CNx-T-SiC contain such kind of CNTs.

4. Resume and conclusions

Three different kinds of CNx samples have been produced using ball-milled slag-SiC material. The elemental composition of the SG-2h revealed that the most abundant elements were Si and Fe. In most cases, the diameter distribution of CNTs presented a bimodal behavior, probably because of a complicated mechanism of agglomeration of catalyst nanoparticles. A spectrum of morphologies was observed depending on the route or synthesis temperature utilized. When SG-2h were used inside the benzylamine, the synthesized samples exhibited N-MWCNTs with large external diameters and short internal diameters possible because of the participation of oxygen in the solution. These synthesized CNx-T revealed the presence of branches or kinks when the synthesis temperature exceeded 800 °C. This situation is like the case when ethanol is mixed with the benzylamine. When SG-2h or SG-SiC are used as catalyst on the quartz tube the morphology can be classified by three primary morphologies: (1) carbon nanotubes with relative small diameters and rugged surfaces with irregular and narrow compartments; (2) carbon nanotubes with large both external and internal diameters, but with two or three sets of multiwall forming complex compartments; (3) completely irregular tubular carbon structures. According to TEM characterizations, CNx-850-SiC presents a peculiar carbon nanotubes type (2). These giant carbon nanotubes present a decorated surface with pieces of nanomaterials composed of carbon or different materials. The encapsulated nanoparticles can be α-Fe or Fe_3C of different shapes and sizes. A significant result is that the nitrogen doping is pyrrolic type in all cases when the synthesis temperature is higher than 850 °C (except for CNx-850-SG). In general, the addition of SiC did not promote N-pyrrolic sites, but it seems that when the synthesis temperature is 850 °C, the effect of SiC for producing pyrrolic nitrogen is crucial. There is no doubt that the best option for producing CNTs with nitrogen atoms immersed in the hexagonal network is by mixing SG-2h with benzylamine. Unfortunately, the benzylamine is damaged by SG-2h which does not allow systematic production using this route. Thus, the best way to manufacture N-MWCNT is by using SG-2h as the substrate preferably at temperatures close to 800. A significant result is the produced CNTs in these cases are attached to catalytic nanoparticles. This feature is not adequate for some applications. However, very recently has been demonstrated that carbon-metal hybrid nanomaterials could be useful for electrochemical applications. Another important result is that SiC could promote the growth of giant carbon nanotubes with unusual internal compartment morphologies. It has been demonstrated here that the catalytic substrate effects are significant to define the morphology of CNTs- if the content of such substrate is altered with SiC giant N-pyrrolic CNTs can be produced.

Acknowledgments

Competing Interests

The authors declare to have no conflict of interest to declare.

Funding

Authors' Contributions

S M V D, V J G, A M G, F T L, E M S fabricated the CNTs and carried out the characterizations. J L F D, A J, and R S S analyzed, discussed, and revised the X P S results. G J L D study and performed the S E M and T E M characterizations. B A R E discussed and analyzed the D R X data. F L U, M T, and E M S supervised the analysis and interpretation of data and worked on the writing and revisions of the manuscript. All authors read, corrected, and approved the final manuscript.

ORCID iDs

Sofía Magdalena Vega-Díaz ⓘ https://orcid.org/0000-0001-6770-6137
Viviana Jehová González ⓘ https://orcid.org/0000-0001-5297-7970
Aarón Morelos-Gómez ⓘ https://orcid.org/0000-0002-5385-8479
Ferdinando Tristán-López ⓘ https://orcid.org/0000-0001-9322-668X
Gladis Judith Labrada-Delgado ⓘ https://orcid.org/0000-0001-5360-9862
Beatriz Adriana Rivera-Escoto ⓘ https://orcid.org/0000-0002-8136-6615
Roque Sánchez-Salas ⓘ https://orcid.org/0000-0001-6393-9152
Alejandro Javier Cortés-López ⓘ https://orcid.org/0000-0002-6467-4595
Juan Luis Fajardo-Díaz ⓘ https://orcid.org/0000-0002-2515-6840
Florentino López-Urías ⓘ https://orcid.org/0000-0003-4001-0038
Mauricio Terrones ⓘ https://orcid.org/0000-0003-0010-2851
Emilio Muñoz-Sandoval ⓘ https://orcid.org/0000-0002-6095-4119

References

[1] Ruoff R S and Lorents D C 1995 Mechanical and thermal properties of carbon nanotubes *Carbon* **33** 925–30
[2] Futaba D N *et al* 2006 Shape-engineerable and highly densely packed single-walled carbon nanotubes and their application as super-capacitor electrodes *Nat. Mater.* **5** 987–94
[3] Das R N, Liu B and Reynolds J R 2009 Rinzler A G Engineered macroporosity in single-wall carbon nanotube films *Nano Lett.* **9** 677–83
[4] Trancik J E, Barton S C and Hone J 2008 Transparent and catalytic carbon nanotube films *Nano Lett.* **8** 982–7
[5] Lau K K S *et al* 2003 Superhydrophobic carbon nanotube forests *Nano Lett.* **3** 1701–5
[6] Qu L, Dai L, Stone M, Xia Z and Wang Z L 2008 Carbon nanotube arrays with strong shear binding-on and easy normal lifting-off *Science* **322** 238–42
[7] Aliev A E *et al* 2009 Giant-stroke, superelastic carbon nanotube aerogel muscles *Science* **323** 1575–8
[8] Hayamizu Y *et al* 2008 Integrated three-dimensional microelectromechanical devices from processable carbon nanotube wafers *Nat. Nanotechnol.* **3** 289–94
[9] Villalpando-Páez F, Romero A H, Muñoz-Sandoval E, Martínez L M, Terrones H and Terrones M 2004 Fabrication of vapor and gas sensors using films of aligned CNx nanotubes *Chem. Phys. Lett.* **386** 137–43
[10] Tran S J, Verschueren A R M and Dekker C 1998 Room-temperature transistor based on a single carbon nanotube *Nature* **393** 49–52
[11] Choi W B *et al* 2001 Ultrahigh-density nanotransistors by using selectively grown vertical carbon nanotubes *Appl. Phys. Lett.* **79** 3696–8
[12] Kong J *et al* 2001 Quantum interference and ballistic transmission in nanotube electron waveguides *Phys. Rev. Lett.* **87** 106801
[13] Datta S S, Strachan D R, Khamis S M and Johnson A T C 2008 Crystallographic etching of few-layer graphene *Nano Lett.* **8** 1912–5
[14] Ci L *et al* 2008 Controlled nanocutting of graphene *Nano Res.* **1** 116–22
[15] Kosynkin D V, Higginbotham A L, Sinitskii A, Lomeda J R, Dimiev A, Price B K and Tour J M 2009 Longitudinal unzipping of carbon nanotubes to form graphene nanoribbons *Nature* **58** 872–6
[16] Cano-Márquez A G *et al* 2009 Ex-MWNTs: graphene sheets and ribbons produced by lithium intercalation and exfoliation of carbon nanotubes *Nano Lett.* **9** 1527–33
[17] Kam N W S, O'Connell M, Wisdom J A and Dai H 2005 Carbon nanotubes as multifunctional biological transporters and near-infrared agents for selective cancer cell destruction *Proc. Natl Acad. Sci.* **102** 11600–5
[18] Iijima S 1991 Helical microtubules of graphitic carbon *Nature* **354** 56–8
[19] Guo T, Nikolaev P, Rinzler A G, Tomanek D, Colbert D T and Smalley R E 1995 Self-assembly of tubular fullerenes *J. Phys. Chem.* **99** 10694–7
[20] Zhang Y and Sun X 2007 Synthesis of carbon nanofibers and foam by catalytic chemical vapor deposition using a water-soluble alkali salt catalyst *Adv. Mater.* **19** 961–4
[21] Baker R T K, Braber M A, Harris P S, Feates F S and White R K 1972 Nucleation and grow of carbon deposits from the nickel catalysed decomposition of acetylene *J. Catal.* **26** 51–62
[22] Baker R T K, Harris P S, Thomas R B and Waite R J 1973 Formation of filamentous carbon from iron, cobalt, and chromium catalyzed decomposition of acetylene *J. Catal.* **30** 86–95

[23] Hofmann S *et al* 2007 *In situ* observations of catalyst dynamics during surface-bound carbon nanotube nucleation *Nano Lett.* **7** 602–8

[24] Terrones M, Kamalakaran R, Seegera T and Rühlea M 2009 Novel nanoscale gas containers: encapsulation of N_2 in CN_x nanotubes *Chem. Comm.* **23** 2335–6

[25] Cruz-Silva E *et al* 2008 Heterodoped nanotubes: theory, synthesis, and characterization of phosphorus-nitrogen doped multiwalled carbon nanotubes *ACS Nano* **2** 441–8

[26] Botello-Méndez A *et al* 2008 Controlling the dimensions, reactivity and crystallinity of multiwalled carbon nanotubes using low ethanol concentrations *Chem. Phys. Lett.* **453** 55–61

[27] Stephan O *et al* 1994 Doping graphitic and carbon nanotube structures with boron and nitrogen *Science* **266** 1683–5

[28] Hsu W K *et al* 2000 Boron-doping effects in carbon nanotubes *J. Mater. Chem.* **10** 1425–9

[29] Han W, Bando Y, Kurashima K and Sato T 1999 Boron-doped carbon nanotubes prepared through a substitution reaction *Chem. Phys. Lett.* **299** 368–73

[30] Fagan S B, Mota R, da Silva A J R and Fazzio A 2004 Substitutional Si doping in deformed carbon nanotubes *Nano Lett.* **4** 975–7

[31] Romo-Herrera J M *et al* 2008 An atomistic branching mechanism for carbon nanotubes: sulfur as triggering agent *Angew. Chem. Int.* **47** 2948–53

[32] Lee Y T, Park J, Choi Y S, Ryu H and Lee H J 2002 Temperature-dependent growth of vertically aligned carbon nanotubes in the range 800–1100 °C *J. Phys. Chem. B* **106** 7614–8

[33] Zou G *et al* 2006 Carbon nanofibers synthesis, characterization and electrochemical properties *Carbon* **44** 828–32

[34] Zheng R, Zhao Y, Liu H, Liang C and Cheng G 2006 Preparation, characterization and growth mechanism of platelet carbon nanofibers *Carbon* **44** 742–6

[35] Takenaka S, Ishida M, Serizawa M, Tanabe E and Otsuka K 2004 Formation of carbon nanofibers and carbon nanotubes through methane decomposition over supported cobalt catalysts *J. Phys. Chem. B* **108** 11464–72

[36] Wang H, Terry R and Baker K 2004 Decomposition of methane over a Ni-Cu-MgO catalyst to produce hydrogen and carbon nanofibers *J. Phys. Chem. B* **108** 20273–7

[37] Naghash A R, Xu Z and Etsell T H 2005 Coprecipitation of nickel-copper-aluminum takovite as catalyst precursors for simultaneous production of carbon nanofibers and hydrogen *Chem. Mater.* **17** 815–21

[38] Van der Lee M K, van Dillen A J, Geus J W, Jong K P and Bitter J H 2006 Catalytic growth of macroscopic carbon nanofiber bodies with high bulk density and high mechanical strength *Carbon* **44** 629–37

[39] Behr M J, Mkhoyan K A and Aydil E S 2010 Catalyst rotation, twisting, and bending during multiwall carbon nanotube growth *Carbon* **48** 3840–5

[40] Shpak A P *et al* 2007 Structure and magnetic properties of iron nanowires encased in multiwalled carbon nanotubes *Acta Mater.* **55** 1769–78

[41] Morelos-Gómez A *et al* 2010 Controlling high coercivities of ferromagnetic nanowires encapsulated in carbon nanotubes *J. Mater. Chem.* **20** 5906–14

[42] Bhaviripudi S, Mile E, Steiner S A III, Zare A T, Dresselhaus M S, Belcher A M and Kong J 2007 CVD synthesis of single-walled carbon nanotubes from gold nanoparticle catalysts *J. Am. Chem. Soc.* **129** 1516–7

[43] Durbach S H, Krause R W, Witcomb M J and Coville N J 2009 Synthesis of branched carbon nanotubes using copper catalysts in a hydrogen-filled DC arc discharger *Carbon* **43** 635–44

[44] Cheng J P *et al* 2006 Natural mineral-marine manganese nodule as a novel catalyst for the synthesis of carbon nanotubes *J. Wuhan Univ. Technol.-Mat. Sci. Edit.* **21** 29–31

[45] Lee C J, Park J, Kim J M, Huh Y, Lee J Y and No K S 2000 Low-temperature growth of carbon nanotubes by thermal chemical vapor deposition using Pd, Cr, and Pt as co-catalyst *Chem. Phys. Lett.* **327** 277–83

[46] Destrée A *et al* 2007 Synthesis and characterization of carbon nanotubes grown on montmorillonite clay catalysts *J. Mater. Sci.* **42** 8671–89

[47] Gournis D, Karakassides M A, Bakas T, Boukos N and Petridis D 2002 Catalytic synthesis of carbon nanotubes on clay minerals *Carbon* **40** 2641–6

[48] Sheng S D and Chen X W 2007 Natural lavas as catalysts for efficient production of carbon nanotubes and nanofibers *Angew. Chem. Int.* **46** 1823–4

[49] Mracek J, Fagan R, Stengelin R M and Hesjedal T 2011 Are carbon nanotubes a naturally occurring material ? hints from methane CVD using lava as a catalyst *Curr. Nanosci.* **7** 294–6

[50] Bacsa R R, De Parseval P, Martin F and Serp P 2013 Geomimetic catalysis: From volcanic stones to ultra-selective $Fe–Mo/Al_2O_3–TiO_2$ catalysts for few-walled carbon nanotube production *Carbon* **64** 219–24

[51] Gong K, Du F, Xia Z, Durstock M and Dai L 2009 Nitrogen-doped carbon nanotube array with high electrocatalytic activity for oxygen reduction *Science* **323** 760–4

[52] Sharifi T, Hu G, Jia X E and Wagberg T 2012 Formation of active sites for oxygen reduction reactions by transformation of nitrogen functionalities in nitrogen-doped carbon nanotubes *ACS Nano* **6** 8904–12

[53] Li Y, Zhou Z, Shen P and Chen Z 2009 Spin gapless semiconductor–metal–half–metal properties in nitrogen-doped zigzag graphene nanoribbons *ACS Nano* **3** 1952–8

[54] Li J *et al* 2015 Searching for magnetism in pyrrolic N-doped graphene synthesized via hydrothermal reaction *Carbon* **84** 460–8

[55] Ombaka L M, Ndungu P G and Nyamori V O 2015 Pyrrolic nitrogen-doped carbon nanotubes: physicochemical properties, interactions with Pd and their role in the selective hydrogenation of nitrobenzophenone *RSC Adv.* **5** 109–22

[56] Bulusheva L G *et al* 2015 Controlling pyridinic, pyrrolic, graphitic, and molecular nitrogen in multi-wall carbon nanotubes using precursors with different N/C ratios in aerosol assisted chemical vapor deposition *Phys. Chem. Chem. Phys.* **17** 23741–7

[57] Huang G, Yang L, Ma X, Jiang J, Yu S-H and Jiang H-J 2016 Metal–organic framework-templated porous carbon for highly efficient catalysis: the critical role of pyrrolic nitrogen species *Chem. Eur. J.* **22** 3470–7

[58] Zheng J *et al* 2015 High content of pyridinic- and pyrrolic nitrogen-modified carbon nanotubes derived from blood biomass for the electrocatalysis of oxygen reduction reaction in alkaline medium *Electrochim. Acta* **168** 386–93

[59] Morant C, Andrey J, Prieto P, Mendiola D, Sanz J M and Elizalde E 2006 XPS characterization of nitrogen-doped carbon nanotubes *Phys. Stat. Sol.* **203** 1069–75

[60] Panchakarla L S, Subrahmanyam K S, Saha S K, Govindaraj A, Krishnamurthy H R, Waghmare, U V and Rao C N R 2006 Synthesis, structure, and properties of boron- and nitrogen-doped graphene *Adv. Mater.* **21** 4726–30

[61] Czerw R *et al* 2001 Identification of electron donor states in N-doped carbon nanotubes *Nano Lett.* **1** 457–60

[62] Jia N, Wang L, Liu L, Zhou Q and Jiang Z 2005 Bamboo-like CNx nanotubes for the immobilization of hemoglobin and its bioelectrochemistry *Electrochem. Comm.* **7** 349–54

[63] Xiong W *et al* 2010 3-D carbon nanotube structures used as high performance catalyst for oxygen reduction reaction *J. Am. Chem. Soc.* **132** 15839–41

[64] Murakami T, Sako T, Harima H, Kisoda K, Mitikami K and Isshiki T 2004 Raman study of SWNTs grown by CCVD method on SiC *Thin Solid Films* **464** 319–22

[65] Ci L and Bai J 2004 Novel micro/nanoscale hybrid reinforcement: multiwalled carbon nanotubes on SiC particles *Adv. Mater.* **16** 2021–4

[66] Ci L J, Zhao Z G and Bai J B 2005 Direct growth of carbon nanotubes on the surface of ceramic fibers *Carbon* **43** 883–6

[67] Ci L, Ryu Z, Jin-Phillipp N Y and Rühle M 2007 Carbon nanotubes/SiC whiskers composite prepared by CVD method *Diam. Relat. Mat.* **16** 531–6

[68] Cao A, Veedu V P, Li X, Yao Z, Ghasemi-Nejhad M N and Ajayan P M 2005 Multifunctional brushes made from carbon nanotubes *Nat. Mater.* **4** 540–5

[69] Veedu V P, Cao A, Li X, Ma K, Soldano C, Kar S, Ajayan P M and Ghasemi-Nejhad M N 2006 Multifunctional composites using reinforced laminae with carbon-nanotube forests *Nat. Mater.* **5** 457–62

[70] Li W, Yuan J, Dichiara A, Lin Y and Bai J 2012 The use of vertically aligned carbon nanotubes grown on SiC for *in situ* sensing of elastic and plastic deformation in electrically percolative epoxy composites *Carbon* **50** 4298–301

[71] Román-Manso B, Vega-Díaz S M, Morelos-Gómez A, Terrones M, Miranzo P and Belmonte M 2008 Aligned carbon nanotube/silicon carbide hybrid materials with high electrical conductivity, superhydrophobicity and superoleophilicity *Carbon* **80** 120–6

[72] Takagi D, Hibino H, Suzuki S, Kobayashi Y and Homma Y 2007 Carbon nanotube growth from semiconductor nanoparticles *Nano Lett.* **7** 2272–5

[73] Ahmad I and Islam M 2019 Reinforcing ability and bonding characteristics of multiwall carbonnanotubes and silicon carbide nanoparticles in inductively sintered alumina ceramic hybrid nanocomposites *J. Alloy. Compd.* **788** 219–30

[74] Uzun A 2019 Production of aluminium foams reinforced with silicon carbide and carbon nanotubes prepared by powder metallurgy method *Composites Part B* **172** 206–17

[75] Matsuda K, Norimatsu W, Bao J, Kawarada H and Kusunoki M 2018 In-plane electrical conduction mechanisms of highly dense carbon nanotube forests on silicon carbide *J. Appl. Phys.* **123** 045104

[76] García-Betancourt M L, Vega-Cantu Y I, Vega-Díaz S M, Morelos-Gómez A, Terrones M and Muñoz-Sandoval E 2015 Magnetic and electrical properties of nitrogen-doped multiwall carbon nanotubes fabricated by a modified chemical vapor deposition method *J. Nanomater.* **2015** 587416

[77] Terrones M *et al* 1999 Carbon nitride nanocomposites: formation of aligned CxNy nanofibers *Adv. Mater.* **11** 655–8

[78] Romo-Herrera J M *et al* 2009 The role of sulfur in the synthesis of novel carbon morphologies: from covalent Y-junctions to sea-urchin-like structures *Adv. Funct. Mater.* **19** 1193–9

[79] Hashim D P *et al* 2012 Covalently bonded three-dimensional carbon nanotube solids via boron induced nanojunctions *Sci. Rep.* **2** 363

[80] Lopez-Urias F, Munoz-Sandoval E, Reyes-Reyes M, Romero A H, Terrones M and Moran-Lopez J L 2005 Creation of helical vortices during magnetization of aligned carbon nanotubes *Phys. Rev. Lett.* **94** 216102

[81] Wang X L *et al* 2015 Size-controlled large-diameter and few-walled carbon nanotube catalysts for oxygen reduction *Nanoscale* **7** 20290–8

[82] Eswaramoorthi I and Hwang L P 2007 Anodic titanium oxide: a new template for the synthesis of larger diameter multi-walled carbon nanotubes *Diam. Relat. Mat.* **16** 1571–8

[83] Eswaramoorthi I and Hwang L P 2006 Synthesis and characterisation of larger diameter multi-walled carbon nanotubes over anodic titanium oxide template *Carbon* **44** 2341–4

[84] Mitchell D R, Brown R M Jr, Spires T L, Romanovicz D K and Lagow R J 2001 The synthesis of megatubes: new dimensions in carbon materials *Inorg. Chem.* **40** 2751–5

[85] Terrones M, Kamalakaran R, Seeger T and Ruhle M 2000 Novel nanoscale gas containers: encapsulation of N-2 in CNx nanotubes *Chem. Comm.* **23** 2335–6

[86] Koos A A, Dowling M, Jurkschat K, Crossley A and Grobert N 2009 Effect of the experimental parameters on the structure of nitrogen-doped carbon nanotubes produced by aerosol chemical vapour deposition *Carbon* **47** 30–7

[87] Elías A L *et al* 2005 Production and characterization of single-crystal FeCo nanowires inside carbon nanotubes *Nano Lett.* **5** 467–72

[88] Dresselhaus M S, Jorio A, Hofmann M, Dresselhaus G and Saito R 2010 Perspectives on carbon nanotubes and graphene Raman spectroscopy *Nano Lett.* **10** 751758

[89] Ratso S, Kaarik M, Kook M, Paiste P, Kisand V, Vlassov S, Leis J and Tammeveski K 2018 Iron and nitrogen co-doped carbide-derived carbon and carbon nanotube composite catalysts for oxygen reduction reaction *Chem. Electro. Chem.* **5** 1827–36

[90] Cortés-López A J, Muñoz-Sandoval E and López-Urías F 2019 Oxygenated surface of carbon nanotube sponges: electroactivity and magnetic *Studies ACS-Omega* **4** 18011–22

[91] Ohkubo K, Nanjo T and Fukuzumi S 2006 Photocatalytic electron-transfer oxidation of triphenylphosphine and benzylamine with molecular oxygen via formation of radical cations and superoxide ion *Bull. Chem. Soc. Jpn.* **79** 1489–500

[92] Wu H and Cui Y 2012 Designing nanostructured Si anodes for high energy lithium ion batteries *Nano Today* **7** 414–29

[93] Figueiredo J L and Pereira M F R 2010 The role of surface chemistry in catalysis with carbons *Cata. Today* **150** 2–7

[94] Sánchez-Salas R 2017 *MSc thesis. Potosino Institute of Scientific and Technological Research.* (SLP, SLP, Mex)

[95] Qiao M H, Cao Y, Deng J F and Xu G Q 2000 Formation of covalent Si–N linkages on pyrrole functionalized Si(100)-(2 × 1) *Chem. Phys. Lett.* **325** 508–12

[96] Qiao M H, Tao F, Cao Y and Xu G Q 2003 Adsorption and thermal dissociation of pyrrole on Si(100)-(2 × 1) *Surf. Sci.* **544** 285–94

[97] Li B, Dai F, Xiao Q, Yang L, Shen J, Zhang C and Cai M 2016 Activated carbon from biomass transfer for high-energy density lithium-ion supercapacitors *Adv. Energy Mater.* **6** 1600802

[98] Andrade-Espinosa G, MuñozSandoval E, Terrones M, Endo M, Terrones H and Rangel-Mendez J R 2009 Acid modified bamboo-type carbon nanotubes and cup-stacked-type carbon nanofibres as adsorbent materials: cadmium removal from aqueous solution *J. Chem. Technol. Biotechnol.* **84** 519–24

[99] Ozden S *et al* 2017 Chemically interconnected light-weight 3D-carbon nanotube solid network *Carbon* **119** 142–9

[100] Wang Y, Iqbal Z and Malhotra S V 2005 Functionalization of carbon nanotubes with amines and enzymes *Chem. Phys. Lett.* **402** 96–101

[101] Tang M, Dou H and Sun K 2006 One-step synthesis of dextran-based stable nanoparticles assisted by self-assembly *Polymer* **47** 728

[102] Quanli J, Haijun Z, Suping L and Xiaolin J 2007 Effect of particle size on oxidation of silicon carbide powders *Ceram. Int.* **33** 309–13

[103] Tishchenko I Yu, Ilchenko O O and Kuzema P O 2015 TGA-DSC-MS analysis of silicon carbide and of its carbon-silica precursor *Chemistry, Physics and Technology of Surface* **6** 216–23

[104] Roy J, Chandra S, Das S and Maitra S 2014 Oxidation behaviour of silicon carbide—a review *Rev. Adv. Mater. Sci.* **38** 29–39 (https://www.degruyter.com/view/j/rams?lang=en) Accession Number: WOS:000340982900004

[105] Munoz-Sandoval E, Perea-Lopez N, Lima-Juarez R, Labrada-Delgado G J, Rivera–Escoto B A, Zamudio A, Silva-Pereyra H G, Robles-Avila E and Terrones M 2014 Synthesis, characterization and magnetic properties of Co@ Au core–shell nanoparticles encapsulated by nitrogen-doped multiwall carbon nanotubes *Carbon* **77** 722–37

[106] Muñoz-Sandoval E, Cortes-López A J, Flores-Gómez B, Fajardo-Díaz J L, Sánchez-Salas R and López-Urías F 2017 Carbon sponge-type nanostructures based on coaxial nitrogen-doped multiwalled carbon nanotubes grown by CVD using benzylamine as precursor *Carbon* **115** 409–21

[107] Chiang Y C, Lin W H and Chang Y C 2011 Influence of treatment duration on multiwall carbon nanotubes functionalized by H$_2$SO$_4$/HNO$_3$ oxidation *Appl. Surf. Sci.* **257** 2401